



## Routes to Dissipation under Different Dynamical Conditions

NILS BRÜGGEMANN AND CARSTEN EDEN

*University of Hamburg, Hamburg, Germany*

(Manuscript received 9 October 2014, in final form 22 May 2015)

### ABSTRACT

In this study, it is investigated how ageostrophic dynamics generate an energy flux toward smaller scales. Numerical simulations of baroclinic instability are used with varying dynamical conditions ranging from quasigeostrophic balance to ageostrophic flows. It turns out that dissipation at smaller scales by viscous friction is much more efficient if the flow is dominated by ageostrophic dynamics than in quasigeostrophic conditions. In the presence of ageostrophic dynamics, an energy flux toward smaller scales is observed while energy is transferred toward larger scales for quasigeostrophic dynamics. Decomposing the velocity field into its rotational and divergent components shows that only the divergent velocity component, which becomes stronger for ageostrophic flows, features a downscale flux. Variation of the dynamical conditions from ageostrophic dynamics to quasigeostrophic balanced flows shows that the forward energy flux and therefore the small-scale dissipation decreases as soon as the horizontal divergent velocity component decreases. A functional relationship between the small-scale dissipation and the local Richardson number is estimated. This functional relationship is used to obtain a global estimate of the small-scale dissipation of  $0.31 \pm 0.23$  TW from a high-resolution realistic global ocean model. This emphasizes that an ageostrophic direct route to dissipation might be of importance in the ocean energy cycle.

### 1. Introduction

Turbulent flows in quasigeostrophic balance show a kinetic energy transfer from smaller to larger scales (Charney 1971; Rhines 1977). In contrast, turbulent flows on much smaller scales feature a kinetic energy flux in the opposite direction, that is, from larger toward smaller scales, where the energy is finally dissipated on molecular scales (Kolmogorov 1991). On the other hand, most of the energy input into the ocean occurs on scales characteristic for quasigeostrophic balance, which are much larger than the small-scale regime that features a downscale energy flux. Because of the inverse energy flux on these larger scales, the energy has to be dissipated at the basin scale. Several mechanisms have been discussed for such a large-scale dissipation, for example, bottom friction (Arbic et al. 2009), lee-wave generation (Bell 1975; Nikurashin and Ferrari 2011), topographic inviscid dissipation of balanced flow (Dewar and Hogg 2010), loss of balance

resulting from Lighthill radiation of gravity waves (Ford et al. 2000), gravity wave drag on the balanced flow (Müller 1976), or direct generation of unbalanced ageostrophic instabilities (Molemaker et al. 2005).

So far, it is unknown whether these processes of large-scale dissipation are efficient enough to balance the energy input into the ocean by wind and tides (Ferrari and Wunsch 2009). On the other hand, numerical model studies from Capet et al. (2008c) and Molemaker et al. (2010) suggest that there is also a direct route to dissipation for the energy of the large-scale circulation, since they observe a downscale energy flux for dynamics that are out of geostrophic balance (but still have a small aspect ratio). However, the importance of this direct route to dissipation in comparison to the indirect dissipation processes on the large scale is not clear so far. A recent study by Barkan et al. (2015) suggests that the direct route might be even more effective than energy loss due to bottom drag. The underlying study aims to come up with a first estimate of the strength of the direct route within the global energy cycle.

Direct observations of a downscale energy flux are difficult since the velocity field has to be measured at a very high spatial resolution to correctly estimate the

*Corresponding author address:* Nils Brüggemann, University of Hamburg, Bundesstrae 53, Hamburg D-20146, Germany.  
E-mail: nils.brueggemann@uni-hamburg.de

energy flux. Scott and Wang (2005) use data from satellite altimetry to estimate the energy flux associated with the geostrophic surface velocities. Since geostrophic velocities are expected to feature an upscale kinetic energy flux, it is arguable if a downscale energy flux can be investigated by satellite data. Consequently, the energy flux estimated by Scott and Wang (2005) is predominantly toward larger scales, and a downscale energy flux found by Scott and Wang (2005) at smaller scales might be attributed to an inadequate resolution of the satellite altimeter (Arbic et al. 2013). Nagai et al. (2009) find enhanced dissipation on the cyclonic side of the Kuroshio Front during a period of frontogenesis that they associate with a downscale energy transfer as found by Capet et al. (2008c) and Molemaker et al. (2010). Indirect evidence for small-scale dissipation triggered by larger-scale dynamics is reported by D'Asaro et al. (2011). Using data obtained from a Lagrangian float and a towed profiling vehicle, D'Asaro et al. (2011) find increased dissipation rates at a front that is subject to downfront winds. They hypothesize that energy is released from the front to small-scale turbulence and dissipation.

To estimate the strength of the direct route to dissipation, it is necessary to investigate which dynamical conditions favor a downscale kinetic energy flux. Therefore, we examine the dependency between the strength of the downscale kinetic energy flux and the dynamical characteristics of the flow system. Molemaker et al. (2010) find that a model based on the full non-hydrostatic equations dissipates substantially more energy at smaller scales than a quasigeostrophic model does for the same dynamical conditions. They also observe a downscale energy flux featured by the nonhydrostatic model, while in the quasigeostrophic model, the energy is transferred in the opposite direction toward larger scales as described by Charney (1971). Thus, the occurrence of ageostrophic dynamics seems to play a crucial role for the establishment of a forward energy flux.

To which extent a flow system develops ageostrophic dynamics strongly depends on its inherent dynamics. A suitable characterization can be given by the Richardson number  $Ri$ , which is the ratio of the vertical density stratification and the vertical shear of the horizontal velocity. While a flow with  $Ri < 1$  is unstable with respect to symmetric instabilities and for  $Ri < 0.25$  also to Kelvin–Helmholtz instabilities, instabilities that arise for  $Ri \gg 1$  are mainly in quasigeostrophic balance (see, e.g., Stone 1966). For  $Ri = O(1)$ , Molemaker et al. (2005) find the dominant unstable mode to be unbalanced to approximately 10%, while additional modes also occur that are unbalanced to an even higher degree.

Values of  $Ri = O(1)$  can be found at the ocean surface with weak stratification or within strong boundary currents with large velocity shears. Simulations of an idealized subtropical, eastern boundary current system by Capet et al. (2008a) and Capet et al. (2008b) reveal submesoscale eddies and filaments out of geostrophic balance in the upper 100 m. Furthermore, Capet et al. (2008c) observe that these unbalanced motions are accompanied by a forward energy flux at spatial scales smaller than the mesoscales (defined by the length scale of the first baroclinic Rossby radius). In contrast, the energy flux is negative at the mesoscales as expected from the theory of geostrophic turbulence (Charney 1971).

The different directions of the energy fluxes are interpreted by Waite and Bartello (2006) and Lindborg (2006) as a competition between quasigeostrophic and stratified turbulence. The former features an upscale energy transfer and a characteristic dependency of the kinetic energy spectrum on the horizontal wavenumber of  $k^{-3}$  (Charney 1971). Observations of the atmospheric kinetic energy spectrum from Nastrom and Gage (1985) indeed show the predicted spectral dependency of  $k^{-3}$  at global scales. However, at smaller scales, the energy spectrum flattens and converges to a spectral slope of  $k^{-5/3}$ . Observations and theoretical studies [see, e.g., Lindborg (2006) and references therein] give support to the hypothesis that the  $k^{-5/3}$  dependency can be explained by a forward cascade due to nonlinearly interacting gravity waves (Dewan 1997). Idealized simulations for stratified turbulence indeed feature a downscale energy flux and a  $k^{-5/3}$  dependency of the spectral kinetic energy density (e.g., Waite and Bartello 2004; Lindborg 2006). In between the regimes of quasigeostrophic turbulence and stratified turbulence, it is not a priori clear whether the upscale energy flux of the quasigeostrophic turbulence or the downscale energy flux of the stratified turbulence dominates. Lindborg (2005) finds that a dominant upscale energy transport occurs as soon as the Rossby number ( $Ro$ ) of the flow is smaller than 0.1.

A competing approach to explain the different characteristics of the energy spectrum results from surface quasigeostrophic dynamics (SQG) (Blumen 1978; Tulloch and Smith 2009). Numerical simulations with a primitive equation model by Klein et al. (2008) point to a strong resemblance between the surface kinetic energy spectrum and the spectrum of the density variance at the surface as suggested by SQG. On the other hand, Klein et al. (2008) find a strong deviation of the interior dynamics from the surface dynamics. Especially, they observe different characteristics of the interior kinetic energy spectrum than predicted from SQG. Therefore, it

is arguable whether SQG dynamics can be used to explain interior flow characteristics (LaCasce 2012).

In this study, we perform simulations of baroclinic instability in a channel. By varying dynamical conditions of this flow from  $Ri = O(10^3)$  to  $Ri = O(1)$ , we aim to observe the transition between an upscale energy flux for quasigeostrophic dynamics to a downscale energy flux for ageostrophic dynamics. An equilibrium in the simulation is achieved by counterbalancing the eddy restratification process with a restoring of the zonal-mean buoyancy toward a target buoyancy. This permanent source of available potential energy (APE) parameterizes forcing in the ocean acting on large scales and balances the conversion of available potential energy into kinetic energy by baroclinic production. The kinetic energy injected by baroclinic production has to be balanced by some kind of dissipation and we apply two different kinds of kinetic energy dissipation. Momentum dissipation by a linear drag of the zonal-mean velocity field acts predominantly on the largest scales. This kind of dissipation is a surrogate of any dissipation mechanism that acts on large-scale flows in geostrophic balance, for example, bottom friction (Arbic et al. 2009), topographic inviscid dissipation of balanced flow (Dewar and Hogg 2010), lee-wave generation (Bell 1975; Nikurashin and Ferrari 2011), Lighthill radiation of gravity waves (Ford et al. 2000), gravity wave drag on the balanced flow (Müller 1976), or ageostrophic instability (Molemaker et al. 2005). On the other hand, dissipation by viscous friction extracts energy predominantly on the smallest resolved scales and is intended to be a parameterization for processes that generate downscale energy fluxes toward molecular scales as in a large-eddy simulation (LES) closure. The energy dissipation rates due to the large- and small-scale dissipation as well as the spectral energy flux for different  $Ri$  are compared to observe differences in the magnitude and direction of the energy flux for quasigeostrophic and ageostrophic dynamics.

In a second setup, we briefly investigate the spectral kinetic energy flux in nearly adiabatic spindown simulations. In these simulations, we do not use the diabatic buoyancy restoring. The simulations do not equilibrate anymore, and ensemble integrations are used to increase the statistical reliability. With this setup, we aim at investigating whether a downscale kinetic energy flux for ageostrophic dynamics can also be found in a nearly adiabatic environment, which might be closer to the interior dynamics of the ocean.

Capet et al. (2008c) find an increase in the forward energy flux for an increasing horizontal resolution of their model and emphasize that it is of major importance to adequately resolve ageostrophic processes. To obtain

an accurate resolution of the dynamics for different background conditions, we adjust the horizontal basin scale in such a way that for each configuration eight of the most unstable waves (Stone 1966) fit into the domain. Thus, we do not need to increase the number of grid points in the model and always use adequate grid resolution. Another difference of our approach in comparison to Capet et al. (2008c) is that we are able to directly investigate different dynamical regimes isolated from any interference between these dynamics and influences from other processes inherent in any more complex model like that one used in Capet et al. (2008c).

Molemaker et al. (2010) compare the dynamics of the quasigeostrophic model with that of a nonhydrostatic model. The present study is an alternative approach to that. Instead of a priori excluding any ageostrophic effects, we allow ageostrophic dynamics in all simulations but rather change the dynamical conditions from a quasigeostrophic to an ageostrophic flow. We are also able to investigate intermediate regimes in between the extrema of ageostrophic flows and flows in quasigeostrophic balance. Waite and Bartello (2006), Lindborg (2006), and Deusebio et al. (2013) investigate the transition between stratified and quasigeostrophic turbulence in the meteorological context. In all those studies, however, the spatial scale and strength of the kinetic energy source is prescribed. The approach of this study is complementary. We aim to investigate baroclinic instability as one of the main sources of turbulence in the ocean. Therefore, the strength and scale of the kinetic energy source is directly related to the dynamics. By varying  $Ri$  throughout different simulations, we examine a wide range of dynamical conditions typical for the ocean meso- and submesoscale regime.

From idealized model studies, we diagnose the small-scale dissipation due to an ageostrophic downscale energy flux in dependence on  $Ri$  and the buoyancy production by baroclinic instability. Furthermore, we estimate a functional relationship between these three quantities and use this to estimate the potential dissipation due to a downscale energy flux in a realistic ocean model ( $1/10^\circ$  horizontal resolution) providing a global estimate of the energy dissipation induced by a downscale energy flux.

This paper is organized as follows: In section 2, we introduce the numerical model and analyze the energy budget in physical and spectral space. An investigation of the energy fluxes under different dynamical conditions can be found in section 3. The influence of these different dynamical conditions on the dissipation is discussed in section 4. In section 5, we discuss the sensitivity of our results with respect to certain model parameters. In section 6, we discuss a nearly adiabatic

spindown scenario through the switching of the buoyancy restoring. An estimate of the energy that might be transferred toward and thus dissipated at small scales is given in section 7. Finally, we end with a summary and conclusions in section 8.

## 2. Diagnosing the energy cycle

### a. The numerical model

We use a configuration of the hydrostatic version of the MITgcm (Marshall et al. 1997). The model domain consists of a reentrant channel with periodic boundary conditions in zonal direction and solid walls at the meridional boundaries. Baroclinically unstable conditions are provided by a vertically sheared and stratified background flow that is in thermal wind balance with a constant meridional buoyancy gradient  $M_0^2$  and a constant stratification  $N_0^2$ . The parameters  $N_0^2$  and  $M_0^2$  determine the Richardson number  $Ri_0$  as follows:<sup>1</sup>

$$Ri_0 = \frac{N_0^2 f^2}{M_0^4}, \quad (1)$$

where  $f$  is the Coriolis parameter. We achieve different  $Ri_0$  and thus different dynamical conditions by varying  $N_0$  for a constant Coriolis parameter  $f = 7 \times 10^{-5} \text{ s}^{-1}$  and a constant meridional stratification  $M_0^2 = 4f^2$ . Since we use a linear equation of state and only temperature as an active tracer, temperature and buoyancy are equivalent.

Following Stone (1966), the fastest exponential growth rate  $\sigma_{\max}$  with respect to the Richardson number for a background state with constant vertical and meridional stratification are given for perturbations with a characteristic length scale  $L_0$ . The length scale and growth rate of this fastest-growing mode are approximately given by

$$L_0 = 2\pi \sqrt{\frac{2}{5}} \sqrt{1 + Ri_0} \frac{M_0^2}{f^2} H, \quad \sigma_{\max} = \sqrt{\frac{5}{54}} \frac{1}{\sqrt{1 + Ri_0}} f, \quad (2)$$

where  $H$  denotes the basin depth that we choose to be  $H = 200 \text{ m}$  throughout all simulations. To achieve

an adequate resolution for different flow scenarios, we choose the basin width to be  $8L_0$  in the zonal and meridional direction. Therefore, eight wavelengths of the most unstable baroclinic waves fit in the domain for every chosen  $Ri_0$ . We use a resolution of  $256 \times 256 \times 40$  grid points in the zonal, meridional, and vertical directions in each model configuration.

The baroclinic eddy field will restratify the ocean front. We aim to prevent this frontal collapse by applying a restoring of the zonal-mean buoyancy to the initial buoyancy. Therefore, we add the term  $\lambda_b(b_0 - \bar{b})$  to the buoyancy tendency where  $\lambda_b$  denotes an inverse time scale that we set to  $\lambda_b = 2\sigma_{\max}$ ,  $\bar{b}$  denotes the zonally averaged buoyancy in the model, and  $b_0$  is a target buoyancy specifying the desired  $Ri_0$  and  $M_0^2$ . This zonal-mean buoyancy restoring yields a permanent source of potential energy that is dissipated by numerical diffusion of the applied third-order upwind advection scheme for temperature and that is transformed into kinetic energy by baroclinic eddies. We do not apply any explicit diffusion. However, we increase the diffusivities in case of statically unstable conditions as a parameterization for convection in the hydrostatic simulations.

To achieve a balanced state, the kinetic energy injected by the baroclinic production has to be balanced by an energy sink. Therefore, we choose two sources of dissipation. The first is due to the biharmonic horizontal and harmonic vertical friction that are most active close to the grid scale. The second is realized by a linear restoring of the zonal-mean horizontal velocity toward a target velocity  $\mathbf{u}_0$  that is in thermal wind balance with the target buoyancy field  $b_0$ . Namely, we add the term  $\lambda_u(\mathbf{u}_0 - \bar{\mathbf{u}}_h)$  to the horizontal momentum equations where  $\lambda_u$  denotes an inverse time scale and  $\bar{\mathbf{u}}_h$  is the zonally averaged horizontal velocity. This second source of dissipation is most active at the basin scale. Since we use free-slip conditions at the sidewalls and at the bottom, the biharmonic dissipation and the zonal drag are the only sinks of kinetic energy. The magnitude of the dissipation is adjusted to a certain  $Ri_0$  by choosing the inverse restoring time scale  $\lambda_u = 0.05\sigma_{\max}$ , the biharmonic viscosity  $A_4 = 1.5 \times 10^{-4} M_0^2 H L_0^3 / f$ , and the harmonic vertical viscosity  $A_v = 1.25 \times 10^{-4} M_0^2 H^2 / f$ .

Although we relax zonal-mean buoyancy, we observe that the equilibrium stratification differs from the initial stratification, and therefore also the mean Richardson number  $Ri$  differs from its initial counterpart  $Ri_0$ . To take this into account for further diagnostics, we determine the global- and time-mean values of  $N^2$  and  $M^2$  within the time period between

<sup>1</sup> We choose  $Ri$  as a control parameter for the difference between geostrophic and ageostrophic dynamics. Another choice might be to use a bulk Rossby number  $Ro = U/(fL)$ , where  $U$  and  $L$  denote a suitable velocity and length scale of the dynamics.  $Ri$  and  $Ro$  can be related by  $Bu = RiRo^2$ , where  $Bu = [NH/(fL)]^2$  is the Burger number. In case of baroclinic instability, a suitable choice for the length scale  $L$  is the Rossby radius  $L = NH/f$ . Then, it follows that  $Bu = 1$ ,  $Ri = 1/Ro^2$ , and that using  $Ri$  is equivalent to using  $Ro$ .

TABLE 1. Overview of characteristic parameters:  $Ri_0 = N_0^2 f^2 / M_0^4$ ,  $Ri = N^2 f^2 / M^4$ ,  $Fr = U_{rms} / (NL_{KE})$ ,  $Fr_\zeta = \zeta_{rms} / N$ ,  $Ro_u = U_{rms} / (fL_{KE})$ ,  $Ro_\zeta = \zeta_{rms} / f$ ,  $Ro_e = P^{1/3} / (L_B^{2/3} f)$ , and  $Re_4 = U_{rms} L_{KE}^3 / A_4$ . Thereby,  $N^2$  and  $M^2$  denote time-mean values of the vertical and meridional stratification, and  $U_{rms}$  and  $\zeta_{rms}$  are the root-mean-square of the horizontal velocity and vertical vorticity component, respectively. The equation  $L_{KE} = 2\pi \int_0^\infty k^{-1} E_{KE} dk / (\int_0^\infty E_{KE} dk)$  denotes a characteristic length scale, and  $P$  is the energy injection at the basin scale  $L_B$  and  $A_4$  the biharmonic viscosity.

$Ri_0$	$Ri$	$Fr_u/10^{-3}$	$Fr_\zeta/10^{-3}$	$Ro_u$	$Ro_\zeta$	$Ro_e$	$N/f$	$Re_4/10^6$
1	12	11	129	0.14	1.7	0.055	22	23
2	16	9.1	101	0.14	1.5	0.048	24	26
4	23	7.5	76	0.14	1.4	0.041	28	29
8	36	5.8	53	0.13	1.2	0.033	33	35
16	64	4.5	37	0.12	1	0.027	40	41
32	102	3	24	0.11	0.84	0.021	47	47
63	186	2.1	15	0.094	0.68	0.016	56	47
126	321	1.3	9	0.076	0.54	0.013	68	55
251	609	0.84	6	0.064	0.44	0.0096	85	61
501	1098	0.47	3	0.048	0.34	0.0074	110	80
1000	1939	0.24	2	0.034	0.25	0.0055	146	100

$20\sigma_{\max}^{-1}$  and  $1200\sigma_{\max}^{-1}$  to calculate a mean  $Ri$  and  $L$  from Eqs. (1) and (2), respectively. In Table 1, we give an overview of important parameters that characterize the flow in the different simulations. We also determine parameters used by, for example, Waite and Bartello (2006) and Lindborg (2005) to characterize their flow dynamics. Considering the criteria of Lindborg (2005) (stratified turbulence occurs above  $Ro_e \approx 0.1$ ) or that of Waite and Bartello (2006) (stratified turbulence occurs above  $Ro_u \approx 0.4$  or  $Ro_\zeta \approx 3$ ), we find that all simulations in Table 1 are still outside the regime of stratified turbulence. However, the experimental design of this study is not intended to necessarily enter this regime but rather to investigate the energy flux for baroclinically unstable flow systems typical for the ocean. Since we observe ageostrophic dynamics for our low  $Ri$  experiments that have a major influence on the energy flux (see below), we consider our configuration adequate.

Snapshots of the vorticity  $\zeta = \partial_x v - \partial_y u$  and the horizontal divergence  $\Delta = \partial_x u + \partial_y v$  of the equilibrated flow system are shown in Fig. 1 for three experiments with different  $Ri$ . The experiment with  $Ri = 12$  features large local Rossby numbers  $\zeta/f$ , especially in the cyclonic spiral-shaped eddies (Fig. 1a). In addition, large values of  $\Delta$  indicate strong up- and downwelling that is characteristic for ageostrophic dynamics (Fig. 1d). In contrast, the experiment with  $Ri = 1939$  shows lower values of both  $\zeta$  and  $\Delta$ , indicating dynamics that are close to quasigeostrophic balance. While the experiments with small  $Ri$  might be representative for the ocean mixed layer

with weak stratification, or for strong boundary currents,<sup>2</sup> larger  $Ri$  might be found in weakly sheared near-surface conditions during summer or within the ocean interior.

### b. The energy cycle in physical space

In this section, we analyze differences in the energy dissipation between experiments with ageostrophic dynamics (small  $Ri$ ) and quasigeostrophic dynamics (large  $Ri$ ). For a dominant downscale energy flux for ageostrophic dynamics, we expect the dissipation by the viscous friction to be larger in comparison to experiments with quasigeostrophic dynamics. The momentum equation in our model is given by

$$\partial_t \mathbf{u}_h = -\nabla \cdot \mathbf{u} \mathbf{u}_h - f \mathbf{k} \times \mathbf{u}_h - \nabla_h p + \lambda_u (\mathbf{u}_0 - \overline{\mathbf{u}_h}) + \mathbf{D}_u, \quad (3)$$

where  $\mathbf{u} = (u, v, w)^T$  denotes the full and  $\mathbf{u}_h$  denotes the horizontal velocity;  $\mathbf{k}$  denotes the unit vector in the vertical direction;  $\nabla_h p$  is the horizontal pressure gradient divided by a reference density;  $\overline{\mathbf{u}_h}$  is the zonal-mean velocity; and  $\mathbf{D}_u$  is the dissipation by the horizontal biharmonic and vertical harmonic dissipation. A kinetic energy (KE) equation is obtained by multiplying Eq. (3) with  $\mathbf{u}_h$ , which, for  $K = \mathbf{u}_h^2/2$ , yields

$$\begin{aligned} \partial_t K = & -\nabla \cdot \mathbf{u} K - \nabla \cdot \mathbf{u} p + w b' \\ & + \mathbf{u}_h \cdot \lambda_u (\mathbf{u}_0 - \overline{\mathbf{u}_h}) + \mathbf{u}_h \cdot \mathbf{D}_u, \end{aligned} \quad (4)$$

where the hydrostatic relation ( $\partial_z p = b$ ) was used and where  $p' = p - N_m^2 z^2/2$  and  $b' = b - N_m^2 z$ , with  $N_m^2$  denoting a global- and time-mean reference stratification of the equilibrated flow (see below).

A conservation equation for APE can be obtained from the conservation equation of buoyancy

$$\partial_t b = -\nabla \cdot \mathbf{u} b + \lambda_b (b_0 - \overline{b}) + D_b, \quad (5)$$

where  $\overline{b}$  denotes the zonal-mean buoyancy, and  $D_b$  denotes numerical diffusion. The latter is related to the third-order upwind advection scheme for buoyancy that is known to be responsible for numerical diffusion<sup>3</sup> and

<sup>2</sup> For  $Ri < 1$ , different kinds of instability next to baroclinic instability are possible like, for example, symmetric instability, Kelvin–Helmholtz instability (for  $Ri < 0.25$ ), or convective instability for  $N_0^2 < 0$ . Since these instabilities act to increase  $Ri$  up to  $Ri = 1$  on very short time and length scales, we restrict our analysis to cases where  $Ri > 1$ .

<sup>3</sup> In contrast, we use a centered second-order scheme for momentum advection that conserves second-order moments. Thus, we do not have to care about numerical dissipation in the kinetic energy budget.



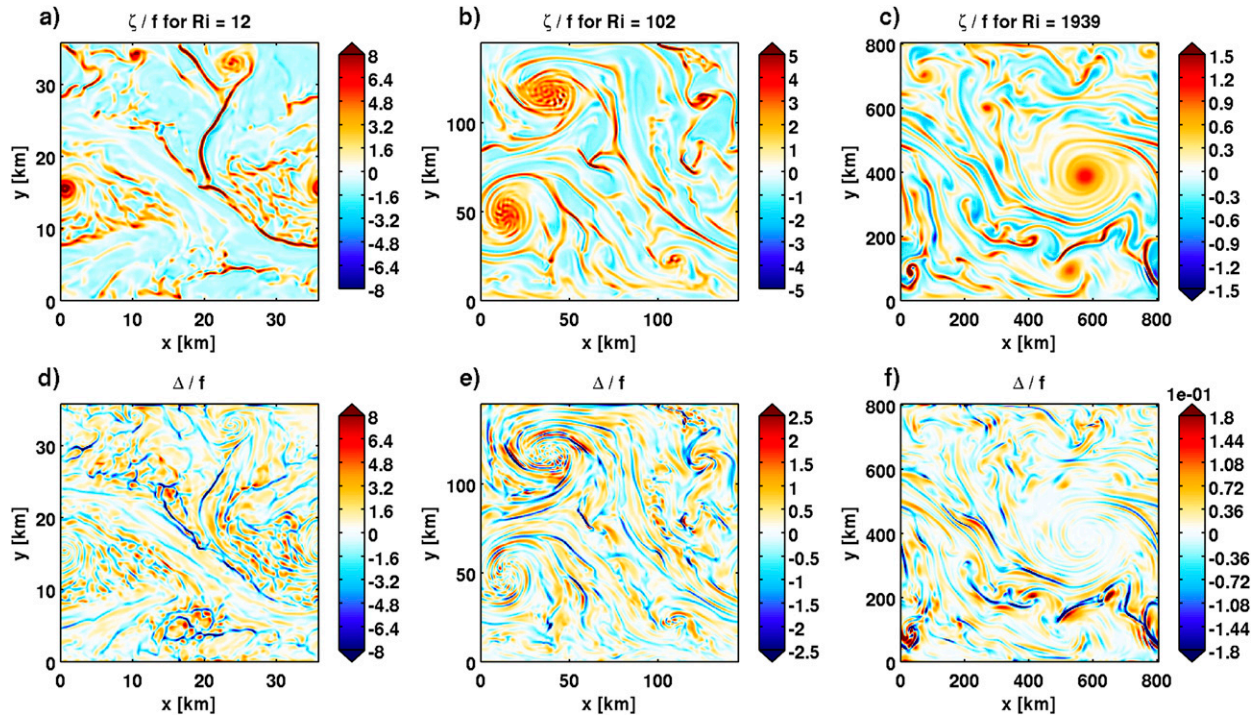


FIG. 1. Snapshots of (a)–(c) surface vorticity and (d)–(f) horizontal divergence at  $t = 1054\sigma_{\max}^{-1}$ , both normalized by  $f$  and shown for times after the flow has equilibrated. (a) and (d) show an experiment with  $Ri = 12$ , (b) and (e) show an experiment with  $Ri = 102$ , and (c) and (f) show an experiment with  $Ri = 1939$ .

convective mixing. Following, for example, [Capet et al. \(2008c\)](#), we determine the former by subtracting the advective tendency of the third-order upwind scheme from the tendency of a second-order centered advection scheme.

We define APE by  $P = b'^2/(2N_m^2)$  with  $b' = b - N_m^2 z$  denoting the difference between the local buoyancy and the reference buoyancy  $N_m^2 z$ . Note that this definition of available potential energy resembles the quasigeostrophic APE where vertical variations of  $b'$  are assumed to be much smaller than the background stratification, in order to neglect the vertical advection of  $b'$ . However, here this is not necessary and  $P$  represents a valid local potential energy also for nonquasigeostrophic dynamics ([Lindborg 2006](#); [Molemaker et al. 2010](#)). The conservation equation for APE is then obtained by multiplying Eq. (5) by  $b'/N_m^2$

$$\partial_t P = -\nabla \cdot \mathbf{u}P - b'w + \frac{b'}{N_m^2} \lambda_b (b_0 - \bar{b}) + \frac{b'}{N_m^2} D_b. \quad (6)$$

Note that there is an exchange between kinetic and available potential energy by the term  $-b'w$  on the right-hand side of Eq. (6) that we refer to as baroclinic production.

To quantify the energy fluxes between the mean and eddy circulation, we perform a further decomposition of the energy cycle. We define mean quantities by zonal averages and eddy quantities by a deviation of the local quantities from their corresponding zonal means. The balance for the mean kinetic energy (MKE) is thus obtained by multiplying Eq. (3) with the zonal-mean velocity and applying a zonal average afterward. Correspondingly, we obtain a balance for the eddy kinetic energy (EKE) by multiplying Eq. (3) with the eddy velocity before we take the zonal average. Budgets for the mean available potential energy (MPE) and the eddy available potential energy (EPE) are obtained likewise by multiplying Eq. (5) by the mean buoyancy and the deviation buoyancy, respectively, before averaging the resulting equations zonally. Sinks, sources, and exchanges between these four energy reservoirs are called the Lorenz cycle ([Lorenz 1955](#)). The magnitude of the energy fluxes are depicted in [Fig. 2](#) for three experiments with different  $Ri$ .

More than 75% of the energy injected in the model is directly transferred from MPE over EPE to EKE with only a negligible exchange between MPE and MKE and a small loss of EPE due to numerical and implicit diffusion. One part of the incoming EKE flux by baroclinic production is dissipated by the viscous friction,

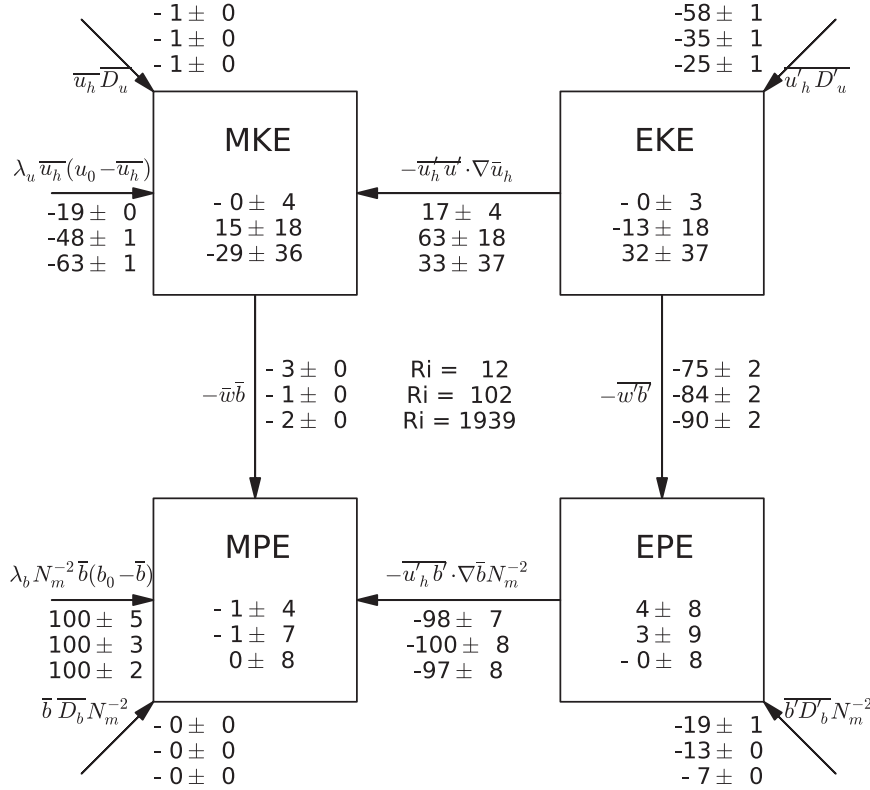


FIG. 2. Lorenz energy cycle for three experiments with different  $Ri$  (12, 102, and 1939). Energy sources, sinks, and exchanges are indicated by arrows. The numbers indicate the magnitude of the energy fluxes in percentage relative to the energy source of the model due to the zonal-mean buoyancy restoring. The horizontal ingoing arrows denote large-scale sources and sinks due to the zonal-mean drag and the zonal restoring. Note that these terms are by definition identically zero for the eddy energy reservoirs. Diagonal ingoing arrows denote sinks due to the viscous friction for the kinetic energy reservoirs and are due to numerical and implicit diffusion for the available potential energy reservoirs. Arrows between the boxes denote energy exchanges between the respective reservoirs. Positive numbers denote an energy exchange in the direction of the respective arrows; negative values indicate an exchange in the opposite direction. Values in the center of the boxes denote the residuals of all incoming and outgoing fluxes. All values are time averages with 95% bootstrapped confidence intervals taken from time series between  $20\sigma_{\max}^{-1}$  and  $1200\sigma_{\max}^{-1}$ .

while the residual is transferred to MKE by an upscale kinetic energy flux. This upscale kinetic energy flux is stronger for larger  $Ri$ . Note that the transfer between EKE and MKE is presumably biased by strong temporal fluctuations. However, the transfer toward MKE certainly increases for increasing  $Ri$  if it is calculated as the residual of the remaining energy transfer terms. Correspondingly, the dissipative energy loss due to the viscous friction of EKE is smaller and the dissipative energy flux of MKE due to the zonal-mean drag is stronger for larger  $Ri$ . This indicates that an energy transfer toward smaller scales and thus an increased dissipation of EKE is more efficient if  $Ri$  is small. For larger  $Ri$ , however, this route to dissipation becomes more and more inefficient, and the energy has to be dissipated at larger

scales; thus, it has to be taken from the reservoir of MKE instead of that of EKE.

### c. The energy cycle in wavenumber space

To diagnose at which spatial scales the specified energy sources and sinks act, we spectrally decompose the kinetic energy balance and consider equations for the spectral kinetic and available potential energy density  $E_{KE}$  and  $E_{APE}$ , respectively. We apply a horizontal Fourier transformation to Eq. (3) and multiply by  $\hat{\mathbf{u}}_h^*$ , where we denote a Fourier transformed quantity by a caret and its complex conjugated counterpart by a star. After taking a global average, we obtain an equation for the spectral density  $E_{KE} = 1/(2H\Delta k) \int \hat{\mathbf{u}}_h^* \cdot \hat{\mathbf{u}}_h dz$  (e.g., Frisch 1995), with  $\Delta k$  denoting a wavenumber increment:

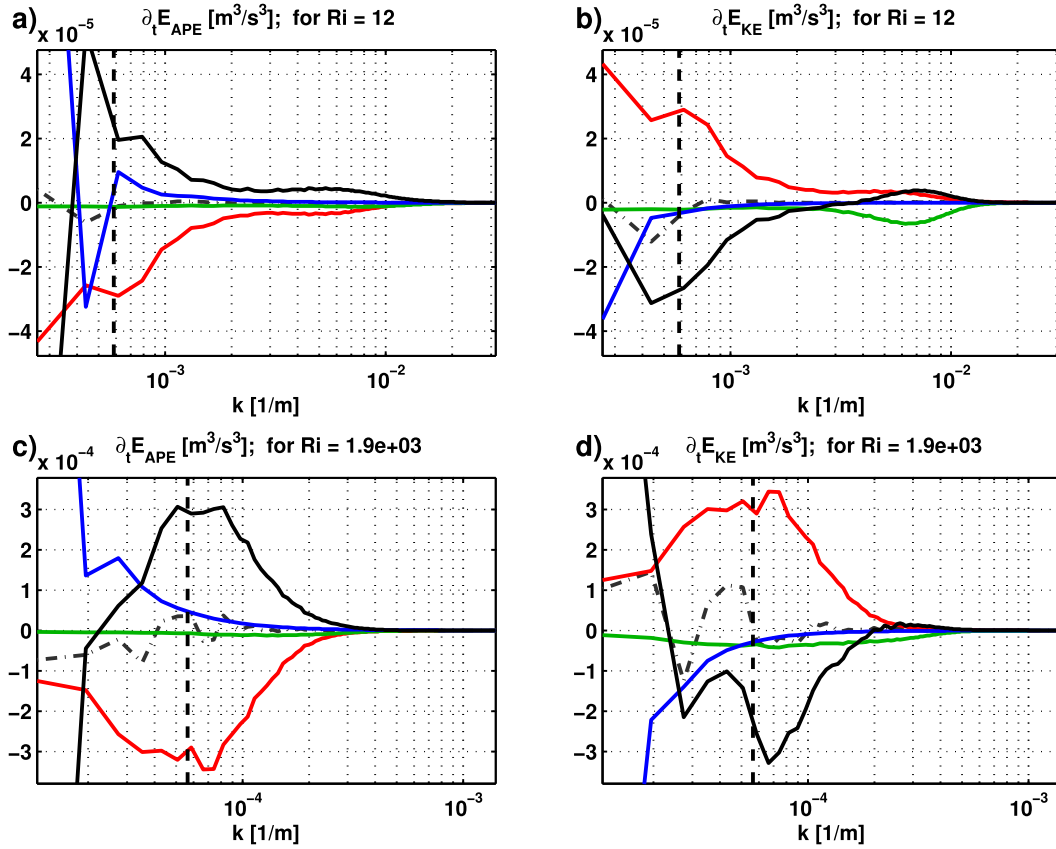


FIG. 3. Tendencies for (a)  $E_{APE}$  and (b)  $E_{KE}$  as a function of the horizontal wavenumber  $k = \sqrt{k_x^2 + k_y^2}$  for a simulation with  $Ri = 12$ . Black curves in (a) and (b) denote tendencies due to advection; red curves denote buoyancy production; green curves denote dissipation due to diffusion in (a) and due to viscous friction in (b); blue curves denote the restoring of zonal-mean buoyancy in (a) and the zonal-mean drag in (b); and dashed-dotted black lines indicate the sum of all terms in (a) and (b), respectively. (c),(d) As in (a) and (b), but for an experiment with  $Ri = 1939$ . In addition, the length scale of the fastest-growing mode  $1/L$  is indicated by vertical black dashed lines in (a)–(d).

$$\partial_t E_{KE} = \frac{1}{H} \int \left[ -\widehat{\mathbf{u}}_h^* \cdot \widehat{\nabla} \cdot \widehat{\mathbf{u}} \mathbf{u}_h - \widehat{\mathbf{u}}^* \cdot \widehat{\nabla} p' + \widehat{\omega}^* \widehat{b}' + \widehat{\mathbf{u}}_h^* \cdot \lambda_u (\widehat{\mathbf{u}}_0 - \widehat{\mathbf{u}}_h) + \widehat{\mathbf{u}}_h^* \cdot \widehat{\mathbf{D}}_u \right] dz \quad (7)$$

(a more detailed derivation can be found in the [appendix](#)). Likewise, we obtain an equation for the spectral density of available potential energy

$E_{APE} = 1/(2N_m^2 H \Delta k) \int \widehat{b}'^* \widehat{b}' dz$  by multiplying the Fourier transform of Eq. (5) by  $\widehat{b}'^*/N_m^2$  and taking the global average:

$$\partial_t E_{APE} = \frac{1}{N_m^2 H} \int \left[ -\widehat{b}'^* \widehat{\nabla} \cdot \widehat{\mathbf{u}} b' - \widehat{b}'^* \widehat{\omega} N_m^2 + \widehat{b}'^* \lambda_b (\widehat{b}_0 - \widehat{b}) + \widehat{b}'^* \widehat{D}_b \right] dz. \quad (8)$$

Note that all terms in Eqs. (7) and (8) are real quantities. As in Eqs. (4) and (6), the buoyancy production  $\widehat{b}'^* \widehat{\omega} = \widehat{\omega}^* \widehat{b}'$  yields an exchange between  $E_{KE}$  and  $E_{APE}$  since it occurs with opposite signs in Eqs. (7) and (8).

Figure 3 shows the budget for spectral kinetic and available potential energy density in correspondence with Eqs. (7) and (8), respectively. As mentioned above,

the only energy source of the model results from the restoring of zonal-mean buoyancy that increases APE on the largest scales (see Figs. 3a,c). Since dissipation is rather small in the  $E_{APE}$  budget, the main loss of  $E_{APE}$  results from baroclinic production converting  $E_{APE}$  into  $E_{KE}$  mainly around the length scale  $L$  of the fastest-growing unstable baroclinic wave. The tendency due to



APE advection is negative on the large forcing scales and positive on the intermediate scales of baroclinic production as can be inferred from Figs. 3a and 3c. Therefore, the nonlinear advection terms in Eq. (8) yield a connection between the large spatial scales of the APE source and the smaller scales where baroclinic production transforms APE into KE. While baroclinic production is largest at the scale of the fastest-growing linear wave  $L$  in the experiment with  $Ri = 1939$ , it shifts toward scales larger than  $L$  for  $Ri = 12$ . Note, however, that the maximum still occurs on scales much smaller than in the experiment with  $Ri = 1939$ .

In contrast to the source of APE, which can be found at the largest scales, baroclinic production increases KE on a wide range of scales. In our model, KE can only be dissipated at large scales by the zonal-mean drag and on the smallest scales by viscous dissipation; therefore, there has to be a transfer of kinetic energy from the intermediate scales of baroclinic production to either the small or the large scales. Figure 3b shows that in the simulation with  $Ri = 12$ , this advection of KE yields a negative tendency of  $E_{KE}$  at large and a positive tendency at small scales. Thus, there has to be a downscale kinetic energy flux in these simulations (which will be discussed in the next section). In the experiment with  $Ri = 1939$ , advection of KE increases  $E_{KE}$  at both large and small scales and decreases EKE at the intermediate scales where baroclinic production is most effective. In this case, the corresponding energy flux has to be downscale at the small but upscale at the large scales. The larger tendencies of the KE advection at large scales indicate that the energy flux is predominantly upscale as might be expected for quasigeostrophic dynamics.

### 3. Energy spectra and fluxes

Figure 3 indicates that an important difference between the dynamics at small and large  $Ri$  is the ratio between the small- and large-scale dissipation. Diagnosing the KE budget in spectral space (Fig. 3) reveals that advection of KE yields a redistribution of energy from intermediate to either small or large scales. To investigate this energy redistribution in dependency on the Richardson number, we consider spectral energy fluxes<sup>4</sup> caused by the advective terms in the energy budget. We derive the spectral kinetic energy flux  $\Pi_{KE}$

and the spectral flux of available potential energy  $\Pi_{APE}$  as follows:

$$\begin{aligned}\Pi_{KE}(k) &= -\frac{1}{H} \int \sum_{k' < k} \widehat{\mathbf{u}}_h^* \cdot \widehat{\nabla} \cdot \widehat{\mathbf{u}}_h \, dz, \\ \Pi_{APE}(k) &= -\frac{1}{H} \int \sum_{k' < k} \frac{1}{N_m^2} \widehat{b}'^* \cdot \widehat{\nabla} \cdot \widehat{\mathbf{u}}_h' \, dz.\end{aligned}\quad (9)$$

A comparison of the spectral densities and fluxes of KE and APE as well as for enstrophy  $\eta = [(\nabla \times \mathbf{u} + f\mathbf{k}) \cdot \nabla b]^2$ , for experiments with different  $Ri$ , illustrates the results of the previous sections. Figure 4a shows that the slope of the KE spectrum is steeper for larger  $Ri$  in the intermediate wavenumber range, approaching a value of approximately  $-3$  that is characteristic for geostrophic turbulence (Charney 1971). For smaller  $Ri$ , the slope in the intermediate wavenumber range comes close to a value of  $-5/3$  as already observed by Capet et al. (2008c) and Molemaker et al. (2010).

As in the case of the spectral KE density, we also find important changes of the spectral KE flux for changing  $Ri$  (Fig. 4e). For small  $Ri$ , the energy flux is positive on all spatial scales and  $\Pi_{KE}$  has a maximum at spatial scales smaller than the length scale  $L$  of the fastest-growing wave. This maximum decreases when  $Ri$  increases, while  $\Pi_{KE}$  becomes negative at larger scales with a minimum at scales larger than  $L$ . Thus, we observe an upscale KE flux as expected from quasigeostrophic turbulence for large  $Ri$  and a downscale KE flux for small  $Ri$ . In between these extrema, there is both a downscale KE flux at smaller and an upscale KE flux at larger scales. Thus, as soon as ageostrophic dynamics begin to become important, the flow is no longer restricted to transfer energy toward larger scales. Instead, the kinetic energy proceeds toward smaller scales providing a direct route to dissipation. These results are in agreement with Capet et al. (2008c) and Molemaker et al. (2010), since both observe a downscale KE flux as soon as ageostrophic dynamics are present and a negative KE flux for dynamics in quasigeostrophic balance. Here, the transition can be directly related to  $Ri$ .

These findings also correspond to results that Lindborg (2006) and Waite and Bartello (2006) obtain for the transition toward stratified turbulence. A comparison of the Rossby numbers  $Ro$  and the Froude numbers  $Fr$  (Table 1) of our low  $Ri$  simulations with the values of, for example, Waite and Bartello (2006) suggests that these simulations are at the lower end of their quasigeostrophic turbulence regime and just about to approach the regime of stratified turbulence. Therefore, it might be argued whether the ageostrophic dynamics in these simulations already cause stratified turbulence,

<sup>4</sup>Note that any interpretation of the energy flux as a local transfer of energy between neighboring scales might be misleading since complex wave-wave (e.g., triad) interactions can be responsible for a nonlocal energy transfer in wavenumber space.

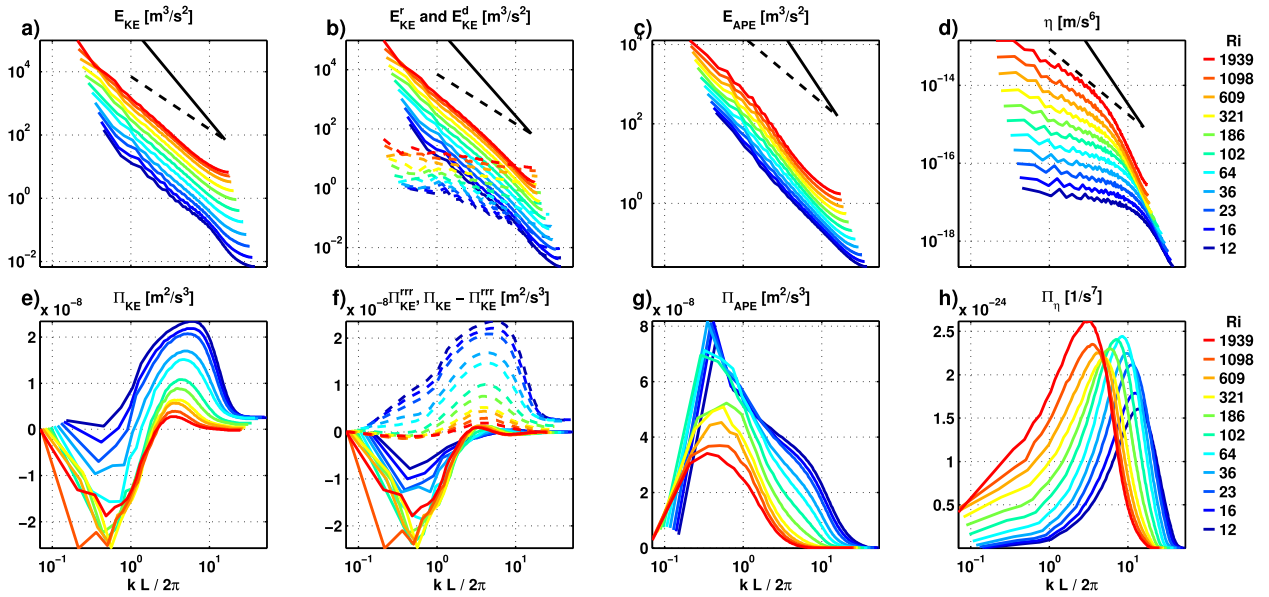


FIG. 4. Energy and enstrophy spectra (a)–(d) and fluxes (e)–(h) as a function of the wavenumber  $k$  scaled by the length scale  $L$  of the fastest-growing mode for different  $Ri$ . Spectra and fluxes for kinetic energy are depicted in (a) and (e). Spectra and fluxes for kinetic energy divided into the rotational component  $E_{KE}^r$  and  $\Pi_{KE}^r$  (solid lines), and the residual component  $E_{KE}^d$  and  $\Pi_{KE} - \Pi_{KE}^r$  (dashed lines) as defined in section 3a are depicted in (b) and (f). Spectra and fluxes for potential energy are depicted in (c) and (g) and for enstrophy in (d) and (h). Different colors of the lines denote experiments with different  $Ri$  as indicated by the legend. Black solid and dashed lines in (a)–(d) denote the spectral slopes of  $-3$  and  $-5/3$ , respectively.

although their spectral characteristics are quite similar to those of stratified turbulence.

Figure 4c shows that in all experiments the spectral slope of APE is in between  $-3$  and  $-5/3$ . In accordance with Molemaker and McWilliams (2010), we find an overall positive flux of APE also for spatial scales and  $Ri$ , where the KE flux changes its sign. In contrast to the APE spectra, the enstrophy spectra shown in Fig. 4d are shallower at larger scales and steepen toward smaller scales. In consistency with Deusebio et al. (2013), we find that the enstrophy flux is positive for all  $Ri$ . Thus, the enstrophy flux is directed toward smaller scales and independent of the direction of the KE flux in all experiments and at all scales. Concerning both the APE and the enstrophy fluxes, we note that the magnitude of the spectral fluxes is not deviating much between the single experiments. The maximum of the APE flux is on scales smaller than  $L$ . In contrast, the maximum of the enstrophy flux is at scales slightly smaller than  $L$  and shifted further toward smaller scales as  $Ri$  decreases.

#### Rotational and divergent components of the energy fluxes

A more detailed interpretation of the energy fluxes and spectra can be obtained if the velocity  $\mathbf{u}$  is decomposed into a rotational part  $\mathbf{u}^r = (u^r, v^r, 0)^T$  and a divergent part  $\mathbf{u}^d = (u^d, v^d, w)^T$  so that  $\partial_x u^r + \partial_y v^r = 0$  and  $\partial_x v^d - \partial_y u^d = 0$  [see also Klein et al. (2008), Capet

et al. (2008c), and Molemaker et al. (2010)]. A decomposition of the spectral kinetic energy density into its rotational component  $E_{KE}^r \equiv 1/(H\Delta k) \int \widehat{\mathbf{u}}_h^{r*} \cdot \widehat{\mathbf{u}}_h^r dz$  and the residual  $E_{KE}^d \equiv 1/(H\Delta k) \int (\widehat{\mathbf{u}}_h^* \cdot \widehat{\mathbf{u}}_h - \widehat{\mathbf{u}}_h^{r*} \cdot \widehat{\mathbf{u}}_h^r) dz$  is shown in Fig. 4b. Except for the smallest scales,  $E_{KE}^r$  is much larger than the residual  $E_{KE}^d$  for all  $Ri$ . Furthermore, the rotational part of the energy spectrum has a much steeper slope for all  $Ri$  than the residual component (Fig. 4b). Note that a spectral slope of  $-3$  would be expected for two-dimensional turbulence (Fjørtoft 1953).

In the same way, the energy flux can be decomposed into one component  $\Pi_{KE}^r$  that is derived by only considering the rotational velocity  $\mathbf{u}^r$  in Eq. (9) and the residual  $\Pi_{KE} - \Pi_{KE}^r$ . If decomposed in this manner, the rotational flow can be considered as nearly two-dimensional. Following the argumentation of Fjørtoft (1953), a two-dimensional flow has to satisfy an additional conservation equation, for enstrophy  $(\zeta^r)^2 = (\partial_x v^r - \partial_y u^r)^2$ , and it thus must obey an inverse energy cascade. In fact,  $\Pi_{KE}^r$  is negative nearly everywhere in all experiments as can be inferred from Fig. 4f. Consequently, any positive part of the kinetic energy flux has to result from components of  $\Pi_{KE}$  that involve the divergent velocity  $\mathbf{u}^d$ . Figure 4f also shows that the residual component  $\Pi_{KE} - \Pi_{KE}^r$  is positive for nearly all scales and for all  $Ri$ .

The decomposition of the velocity field indicates a sharp separation between the dynamics that is caused by

the rotational velocity field and that of the divergent velocity field. The steep kinetic energy spectrum and the upscale kinetic energy flux associated with the rotational velocity are similar to what would be expected for quasigeostrophic turbulence (Charney 1971). In contrast, the relatively flat kinetic energy spectrum and the downscale kinetic energy flux related to the divergent flow agrees well with energy spectra and fluxes observed in stratified turbulence (e.g., Lindborg 2005). For larger Ri, the kinetic energy fluxes seem to be dominated by the rotational part, as one would expect for the limit of quasigeostrophic dynamics where the velocity is to the first order divergence free. For decreasing Ri, the importance of the divergent velocity component increases and changes the main characteristics of the kinetic energy flux, although the magnitude of the divergent kinetic energy is much smaller than its rotational counterpart.

#### 4. Dependency of the energy dissipation on the Richardson number

The findings of the previous section suggest a correlation between the strength of the downscale and upscale kinetic energy flux and the Richardson number. In Fig. 5a, we show the maximum  $\Pi_{\max}$  and the minimum  $\Pi_{\min}$  of the kinetic energy fluxes normalized by  $\Pi_{\max} - \Pi_{\min}$  in dependency on the time- and basin-mean Ri. The normalized  $\Pi_{\max}$  and  $\Pi_{\min}$  represent the ratio of kinetic energy that is redistributed from intermediate to small or large scales, respectively. As discussed in the previous sections, Fig. 5a shows that the downscale kinetic energy flux decreases for increasing Ri and that the opposite is the case for the upscale kinetic energy flux. For  $Ri \approx 35$ , we find that the downscale flux is roughly as strong as the upscale flux ( $\Pi_{\max} = -\Pi_{\min}$ ).

The differences in the energy fluxes for different Ri have a direct influence on the ratio of the large- and small-scale dissipation. If more energy is transferred to larger scales, the large-scale dissipation has to increase and the small-scale dissipation has to decrease in order to achieve equilibrium. The opposite is the case if more energy is transferred toward smaller scales. Figure 5b shows the Richardson dependency of the small- and large-scale kinetic energy dissipation  $D_s$  and  $D_l$ , respectively, normalized by the kinetic energy source due to baroclinic production  $B$ . We define here the small-scale energy dissipation as the global average over the viscous friction and, correspondingly, the large-scale energy dissipation as the dissipation induced by the zonal-mean drag. While the large-scale dissipation increases with increasing Ri, the small-scale dissipation decreases. This finding is in good agreement with the

increase of the upscale kinetic energy flux for larger Ri. The sum of  $D_s/B$  and  $D_l/B$  has to yield one that is approximately the case.

To estimate a functional relationship between Ri and  $D_s/B$  and  $D_l/B$ , we approximate the Ri dependency of  $D_s$  by

$$D_s = [1 - r_{D/B}(Ri - 1)^\gamma]B; \quad (10)$$

correspondingly,  $D_l$  can be obtained by  $D_l = B - D_s$ . For  $Ri = 1$ ,  $D_s = B$  in Eq. (10) such that the kinetic energy flux is completely toward smaller scales. Note that other instability processes like symmetric instabilities or Kelvin–Helmholtz instabilities might occur if  $Ri < 1$ , and Eq. (10) should therefore only be used for  $Ri > 1$ . In Eq. (10),  $r_{D/B}$  denotes the fraction of  $D_l/B$  at  $Ri = 2$ , and  $\gamma$  is an exponential coefficient that determines how strongly  $D_s$  decreases for increasing Ri.

The functional relationship Eq. (10) is best fitted by eye to the diagnosed values  $D_s/B$  and  $D_l/B$  by choosing  $r_{D/B} = 0.1$  and  $\gamma = 0.4$  (see solid lines in Fig. 5b). To give an impression of the sensitivity, we also show curves corresponding to Eq. (10) with  $r_{D/B} = 0.3$  (dashed lines in Fig. 5b) and  $r_{D/B} = 0.5$  (dashed–dotted lines). Note that Eq. (10) seems to yield a reasonable representation of  $D_s/B$  and  $D_l/B$  for  $Ri < 200$ . For larger Ri, however, the diagnosed  $D_s/B$  is underestimated by our choice of parameters. This underestimation might be compensated by a different fit, but since we find hardly any significant downscale energy flux for these large Ri, we assume that the finite values for  $D_l$  at large Ri are artifacts of the biharmonic friction. For reasons of numeric stability it is inevitable to allow for a finite amount of dissipation; also, this dissipation might be unrealistic in reality. Therefore, through the functional relationship given in Eq. (10) and the corresponding parameter choice, we assume a smaller amount of energy dissipated at small scales for large Ri than diagnosed from our model to not overestimate this energy sink.

#### 5. Sensitivity experiments

The three most important parameters that might influence the sensitivity of the energy balance in our idealized model simulations are the buoyancy-restoring coefficient  $\lambda_b$ , the restoring coefficient of the zonal-mean drag  $\lambda_u$ , and the horizontal biharmonic viscosity  $A_4$ . In this section, we discuss the sensitivity of the underlying results with respect to these parameters (a list of the parameter values can be found in Table 2). Since the simulations are computationally quite expensive for a horizontal resolution of  $256 \times 256$  grid points, we perform the sensitivity simulations with the lower resolution of  $120 \times 120$  grid points.

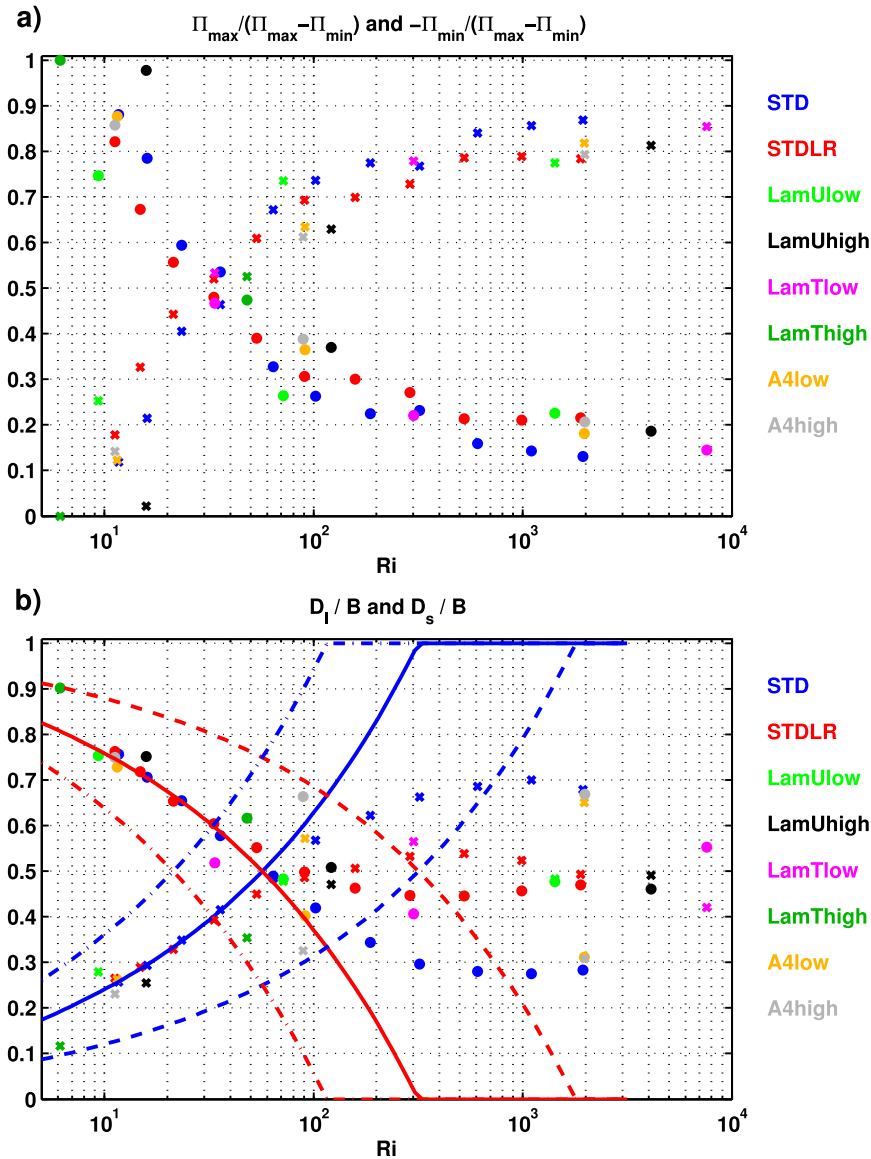


FIG. 5. (a) Maximum  $\Pi_{\max}$  and minimum  $-\Pi_{\min}$  of the kinetic energy flux as a function of  $Ri$  indicated by dots and crosses, respectively. Maxima and minima are normalized by  $\Pi_{\max} - \Pi_{\min}$ . (b) Small-scale dissipation  $D_s$  (dots) and large-scale dissipation  $D_l$  (crosses) normalized by the baroclinic production  $B$ . The solid red line indicates the assumed functional relationship between  $D_s/B$  and  $Ri$  in accordance with Eq. (10). The blue line denotes  $D_l/B = 1 - D_s/B$ . The solid lines are obtained by using  $\gamma = 0.4$  and  $r_{D/B} = 0.1$ . Dashed and dashed-dotted lines indicate sensitivity estimates for  $r_{D/B} = 0.05$  and  $r_{D/B} = 0.15$ , respectively. Different colors in (a) and (b) denote different experiments as indicated by the legend (for details see Table 2).

In Fig. 5, the results of the sensitivity experiments are compared with those of the standard simulation (STD) discussed in the previous sections. The experiments with a reduced horizontal resolution of  $120 \times 120$  grid points (STDLR) show quite similar values for the small- and large-scale dissipation as long as  $Ri$  is small. For  $Ri > 100$ , however, the small-scale dissipation is larger in STDLR, and the large-scale dissipation is smaller in

comparison to STD. In STDLR, a higher biharmonic viscosity  $A_4$  is applied in order to obtain the same grid Reynolds number  $U_0 dx^3/A_4$  as in STD, where  $U_0$  is the magnitude of the zonal background velocity shear multiplied by the water depth. A doubling of the horizontal resolution thus means an 8 times increased  $A_4$ . We assume that this enhanced viscosity leads to a stronger extraction of kinetic energy from the basically

TABLE 2. Parameters of different sensitivity experiments with  $U_0 = M_0^2 H/f$  denoting a velocity scale,  $dx$  is the horizontal, and  $dz$  is the vertical grid size. Note that the mixing of buoyancy is caused by a third-order upwind advection scheme in the buoyancy equation and implicit diffusion in case of static unstable conditions.

Name	$(n_x, n_y, n_z)$	$\lambda_b/\sigma_{\max}$	$\lambda_u/\sigma_{\max}$	$U_0 dx^3/A_4$	$U_0 dz/A_v$	$k_{\max} dx$
STD	(256, 256, 40)	2.0	0.05	2.0	200	0.2
STDLR	(120, 120, 40)	2.0	0.05	2.0	200	0.4
LamUlow	(120, 120, 40)	2.0	0.03	2.0	200	0.4
LamUhigh	(120, 120, 40)	2.0	0.10	2.0	200	0.4
LamTlow	(120, 120, 40)	0.4	0.05	2.0	200	0.4
LamThigh	(120, 120, 40)	10.0	0.05	2.0	200	0.4
A4low	(120, 120, 40)	2.0	0.05	10.0	200	0.4
A4high	(120, 120, 40)	2.0	0.05	0.4	200	0.4

geostrophically balanced velocity field. Since the kinetic energy flux is upscale in STD (Fig. 4e) as in STDLR (not shown) for high Ri, we consider the increased small-scale dissipation as artificial.

Sensitivity experiments with a 5 times higher (A4high) and a 5 times lower (A4low)  $A_4$  support these findings. While the magnitudes of the small- and large-scale dissipation of A4low are comparable to those of STD for all Ri, the magnitude of the small-scale dissipation strongly increases for A4high at high Ri. Thus, we conclude that it is essential that the small-scale dissipation does not interfere too much with the geostrophically balanced scales in order to obtain an unbiased result for the small- and large-scale dissipation. Note that [Arbic et al. \(2013\)](#) find an increased downscale energy flux at small scales even in a quasigeostrophic model as soon as the viscosity is increased. The downscale energy flux and associated small-scale dissipation thus might be overestimated in our simulations with high Ri. However, we do not observe a similar sensitivity for our simulations for experiments with smaller Ri.

Apparently, in all of our simulations, the small-scale dissipation seems to bias the results at higher Ri, while the experiments with lower Ri seem not to be affected. One might circumvent this problem by further increasing the resolution and with this, enabling smaller horizontal viscosities. However, we make no attempt to do so, since we find in all experiments an upscale kinetic energy flux for high Ri. Therefore, we assume that the small-scale dissipation at high Ri is more or less artificial and that the entire kinetic energy has to be dissipated at large scales as indicated by our parameterization of the small- and large-scale dissipation (solid lines in Fig. 5).

The series of experiments with a 5 times higher (LamThigh) and a 5 times lower (LamTlow)  $\lambda_b$  do not change the estimated functional relationship of the small- and large-scale dissipation. The most apparent differences between these simulations and those of STDLR are substantially fewer deviations of Ri from the target  $Ri_0$ . This appears reasonable since any deviations

of the target buoyancy field from the actual buoyancy field and thus deviations of Ri from  $Ri_0$  are more strongly damped if a higher  $\lambda_b$  is chosen. As a consequence, the simulations in LamBhigh have lower Ri and those of LamBlow have higher Ri, although  $Ri_0$  is the same in both series of experiments. Note, however, that the small- and large-scale dissipation seems to adjust to the corresponding Ri and the functional relationship between  $D_s/B$  or  $D_l/B$  and Ri and seems not affected by this.

We discuss the sensitivity of the small- and large-scale dissipation with respect to  $\lambda_u$  by considering a series of experiments with a 2 times increased (LamUhigh) and a 2 times decreased (LamUlow)  $\lambda_u$ . Increasing  $\lambda_u$  results in a stronger damping of the mean flow and thus a reduced velocity shear and a higher Ri. Furthermore, a higher  $\lambda_u$  increases slightly the large-scale dissipation at higher Ri and correspondingly decreases the small-scale dissipation. At lower Ri, the results seem not to be affected by a 2 times increased or decreased  $\lambda_u$ . By increasing  $\lambda_u$  by a factor of 10, we find slightly larger values of  $D_s$  for low Ri (not shown). Note that a downscale energy flux for  $Ri_0 = 1$  is also found for  $\lambda_b = \lambda_u 2\sigma_{\max}$  (not shown). However, our main intention is to give a conservative estimate of the small-scale dissipation; thus, we do not discuss the simulations with the largely increased  $\lambda_u$  in the following.

In summary, we can identify some sensitivities of the strength of the small- and large-scale dissipation on the investigated parameters  $A_4$ ,  $\lambda_b$ , and  $\lambda_u$ . In most cases, however, these sensitivities do not suggest significantly changing the estimated functional relationship between Ri and  $D_s/B$  and  $D_l/B$ . Most important, at small Ri the results are very robust and close to the proposed functional relationship, and larger biases can be found only for large Ri. However, the finding of a downscale kinetic energy flux at small and an upscale kinetic energy flux at large Ri can be found in all sensitivity simulations. This indicates that the sensitivities of the small- and large-scale dissipation at large Ri are rather an effect of the



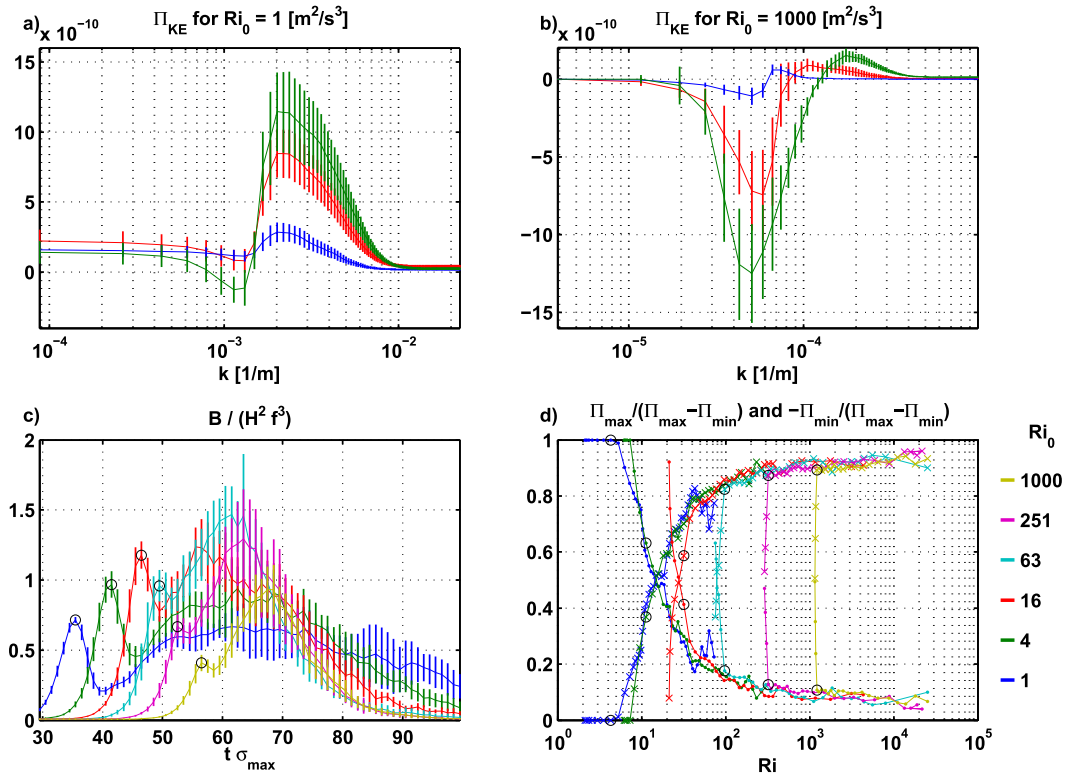


FIG. 6. (a) Kinetic energy fluxes for three different snapshots for an ensemble of 10 experiments with  $Ri_0 = 1$ . (b) As in (a), but for  $Ri_0 = 1000$ . Snapshots are chosen correspondingly to the first maximum of buoyancy production as indicated in (c) (red line), two snapshots before that (blue line), and two snapshots after that (green line). (c) Time series of buoyancy production  $B$  scaled by  $H^2 f^3$ . The first maximum of buoyancy production is indicated by a black circle. The standard deviation of the ensemble spread is indicated in (a)–(c) by vertical lines. (d) Maximum  $\Pi_{max}$  and minimum  $-\Pi_{min}$  of the kinetic energy flux indicated by dots and crosses, respectively, as a function of the time-dependent basin-mean  $Ri$ . Maxima and minima are normalized by  $\Pi_{max} - \Pi_{min}$ . Different colors denote different initial Richardson numbers  $Ri_0$  that are specified in the legend. Black circles indicate the first maximum of  $B$  and correspond to those in (c).

biharmonic friction that appears too large in all simulations. The underlying sensitivity study indicates that an increased horizontal resolution with decreased biharmonic viscosity might resolve this problem. However, the large increase of the computational costs prevents us from further investigating this issue.

## 6. Energy fluxes in adiabatic spindown simulations

The simulations discussed so far contain a diabatic source of energy in the form of the applied buoyancy restoring. Since diabatic energy sources are assumed to be weak in the ocean interior, it is interesting to investigate to which extent a downscale KE flux can also be found in an adiabatic environment. Therefore, we perform similar experiments as before but without any buoyancy restoring. While in these simulations diabatic effects are drastically reduced, the flow does not reach a statistical equilibrium anymore. The eddies flatten the isopycnals and convert APE into KE. The kinetic energy

is finally dissipated by either the small-scale dissipation or the zonal-mean drag. Since there is no process that supplies APE again, the flow finally comes to a rest.

The time dependency of the flow prevents the use of time averages. Instead, we use statistical averages based on an ensemble of 10 simulations each that are identical concerning the background conditions and only differ by random perturbations added to the mean initial buoyancy. Figures 6a and 6b show snapshots of the kinetic energy fluxes  $\Pi_{KE}$  for one ensemble of simulations with  $Ri_0 = 1$  and another one with  $Ri_0 = 1000$ . As before in the equilibrated simulations, we find a downscale kinetic energy flux in the experiments with  $Ri_0 = 1$  and a strong upscale kinetic energy flux together with a weak downscale kinetic energy flux in the experiments with  $Ri_0 = 1000$ .

In contrast to the equilibrated simulations discussed before, the buoyancy production, the energy fluxes, the dissipation rates, and the Richardson number now strongly depend on time. As soon as eddies have developed,

the buoyancy production  $B$  increases as can be inferred from Fig. 6. After reaching a first maximum,  $B$  decreases before increasing again and showing a second maximum. By flattening the isopycnals, the eddies also increase the Richardson number. As a consequence, the length scale of the fastest-growing mode increases in correspondence to Eq. (2). While  $Ri$  increases, the dynamical conditions do not favor the growth of the initially fastest-growing wave anymore. Instead waves with larger and larger wavelengths are favored as the restratification proceeds.

Since the dynamical conditions become more and more quasigeostrophic the stronger the restratification has proceeded, we expect the direction of the energy flux to change from a downscale energy flux for initially small  $Ri$  to an upscale energy flux as soon as  $Ri$  has entered the dynamical regime of quasigeostrophy. To infer the dependency of the energy flux on the time-varying  $Ri$ , we show in Fig. 6d the maximum  $\Pi_{\max}$  and the minimum  $\Pi_{\min}$  of the kinetic energy flux for different experiments with different initial  $Ri_0$  normalized by  $\Pi_{\max} - \Pi_{\min}$  as in Fig. 5a. As expected,  $\Pi_{\max}$  and  $\Pi_{\min}$  change with time. If we consider, for instance, the ensemble with  $Ri_0 = 1$ , we find that  $\Pi_{\max} > -\Pi_{\min}$  during the first phase of restratification. Afterward, during the following phases of restratification where  $Ri$  has already increased over an order of magnitude, the situation changes and  $\Pi_{\max} < -\Pi_{\min}$ . Similarly, we can observe for the ensembles with larger  $Ri_0$  that  $\Pi_{\max}$  decreases and  $-\Pi_{\min}$  increases for increasing  $Ri$ . Independent of  $Ri_0$ , the functional relationship between  $Ri$  and the normalized downscale or upscale kinetic energy flux appears to be the same as in the equilibrated experiments as soon as the buoyancy production  $B$  reaches its maximum; thus, the eddies start to effectively restratify the isopycnals. We find  $\Pi_{\max} = -\Pi_{\min}$  for  $Ri \approx 20$ . Thus, the downscale energy flux is slightly less efficient in the spindown simulations in comparison to the equilibrated simulations where we find  $\Pi_{\max} = -\Pi_{\min}$  for  $Ri \approx 35$ .

## 7. Global estimates of the ageostrophic downscale energy flux

To obtain global estimates of the ageostrophic downscale energy flux, we use data from a simulation with an eddy-permitting ( $1/10^\circ$  horizontal resolution) realistic global ocean model (von Storch et al. 2012). A mean over 10 yr is applied in order to derive the baroclinic production rate  $\overline{w'b'}$ . The global integral of  $\overline{w'b'}$  yields a net energy transfer of 0.73 TW from eddy potential energy into eddy kinetic energy [see von Storch et al. (2012) for a detailed discussion of the eddy energy cycle]. Note that  $\overline{w'b'}$  gets negative at some locations,

indicating a transfer of eddy kinetic to eddy potential energy. However, to assess the small-scale dissipation by the ageostrophic downscale energy flux, it appears reasonable to only consider the energy transfer from eddy potential to eddy kinetic energy and not vice versa. Considering only the positive values of  $\overline{w'b'}$ , the global integral of this eddy kinetic energy source is about 1.65 TW.

The Richardson number  $Ri$  is derived from the model as

$$Ri = \frac{N^2}{(\partial_z \bar{u})^2 + (\partial_z \bar{v})^2}, \quad (11)$$

where  $N^2$ ,  $\partial_z \bar{u}$ , and  $\partial_z \bar{v}$  are the vertical gradients of the mean buoyancy and zonal and meridional velocity, respectively, averaged over 1 day in winter conditions. The reason for choosing a shorter averaging period to derive  $Ri$  results from the assumption that ageostrophic dynamics occur on time scales from hours to days. For longer time averages much of the small-scale variability is averaged out, yielding smoother velocity and buoyancy fields and thus larger  $Ri$ . Therefore, the downscale energy flux is likely to be underestimated if too long time averages are applied in the derivation of  $Ri$ . In fact, the potential energy dissipation reduces by about 50% (not shown) if  $Ri$  is derived from the 10-yr mean velocity and buoyancy fields.

A horizontal and meridional section of  $Ri$  is shown in Figs. 7a and 7b. Low values of  $Ri$  that indicate the potential importance of the downscale energy flux can be found at the surface, in the Southern Ocean, in western boundary currents, and at the equator. However, in most other regions,  $Ri$  is large, indicating quasigeostrophic conditions without significant downscale energy flux. The regions of reduced values of  $Ri$  in the model near the equator, in the Southern Ocean, and in the North Atlantic at roughly 1000-m depth compare well with  $Ri$  calculated from individual CTD sections (not shown). There are also indications in the observations of reduced  $Ri$  values near the bottom of the South Atlantic, as seen in Fig. 7b, but not as pronounced as in the model. Differences between model and observations are larger  $Ri$  maxima in the weakly stratified regions of the Southern Ocean and the abyssal North Atlantic. These differences will not impact our estimate of the energy transfer to small scales very much since it is very low for  $Ri > 300$ , but we note that model problems such as the relatively coarse vertical resolution at depth might impact our estimate here.

By using the estimated functional relationship of Eq. (10), we can estimate the amount of energy that is dissipated at small scales due to the downscale energy flux.

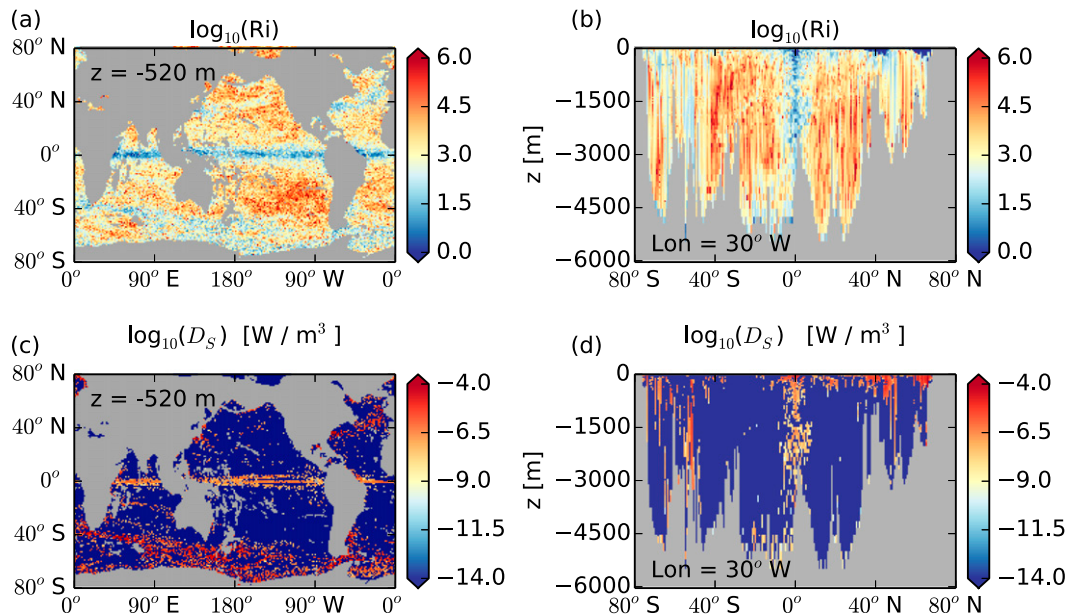


FIG. 7. (a),(b) Horizontal and meridional sections of the logarithm of  $Ri$  determined by Eq. (11) from a daily mean buoyancy and velocity field in winter of a realistic global ocean model (von Storch et al. 2012). (c),(d) Horizontal and meridional sections of the potential small-scale dissipation  $D_s$  derived from Eq. (10) with  $Ri$  determined as described above and  $B$  estimated from 10-yr-averaged buoyancy and velocity fields.

In Figs. 7c and 7d, we show a horizontal and meridional section of the potential small-scale dissipation due to an ageostrophic downscale energy flux  $D_s$  inferred by Eq. (10). High values of  $D_s$  can be found in the Southern Ocean and at the ocean surface of western boundary currents and at the equator. The global integral of  $D_s$  yields a dissipation of 0.31 TW that is 19% of the energy conversion from eddy potential to eddy kinetic energy.

The uncertainty of the previous estimate can be assessed by using different parameter choices for  $r_{D/B}$  and  $\gamma$  in Eq. (10). In Fig. 5, we also show curves for  $r_{D/B} = 0.05$  and  $r_{D/B} = 0.15$ . We use these different parameter choices to infer the uncertainty of the underlying estimate of  $D_s$ . Additionally, we also derive dissipation rates for  $\gamma = 0.3$  and  $\gamma = 0.5$ . The corresponding values of the energy dissipation by the ageostrophic downscale energy flux range from 0.21 to 0.54 TW and all values can be found in Table 3. Note, however, that we include the equator in the estimation, but it is not clear if there is a similar  $Ri$  dependency if the Coriolis force vanishes. Especially since there is no geostrophic turbulence directly at the equator and estimates for large  $Ri$  are likely to fail. On the other hand,  $Ri$  is relatively small at the equator, indicating a downscale energy flux. To check the sensitivity with respect to this caveat, we estimate the potential energy dissipation by the ageostrophic downscale energy flux excluding the latitude band from 5°S to 5°N and find that still 0.26 TW

would be dissipated in the remaining ocean. In the mixed layer,  $N^2$  vanishes or is even negative in the case of static convection. Since there are no attempts made in this study to investigate the small-scale kinetic energy dissipation for  $Ri < 1$ , we set  $Ri$  to one in all estimates for all regions where  $Ri < 1$  applies. By this, we assume that processes like convection or symmetric instabilities yield a restratification on very short time scales that result in dynamical conditions of  $Ri = 1$  (Fox-Kemper et al. 2008). However, to test the sensitivity of our results with respect to this assumption, we also estimate the energy dissipation by excluding all regions where  $Ri \leq 1$  and find that still 0.25 TW are dissipated in the deeper ocean.

TABLE 3. Global integral of the potential energy dissipation (TW) by a potential ageostrophic downscale energy flux inferred from a realistic global ocean general circulation model (von Storch et al. 2012);  $Ri$  is derived by Eq. (11) from daily mean buoyancy and velocity fields. For the STD, NOEq, NoML, and SO cases,  $D_s$  was derived by Eq. (10) with  $\gamma = 0.4$  and  $r_{D/B} = 0.1$ . For rdbL,  $\gamma = 0.4$  and  $r_{D/B} = 0.05$ . For rdbH,  $\gamma = 0.4$  and  $r_{D/B} = 0.15$ . For gamL,  $\gamma = 0.3$  and  $r_{D/B} = 0.1$ . For gamH,  $\gamma = 0.5$  and  $r_{D/B} = 0.1$ . Note also that for NoEq  $D_s$  was derived without the equator domain from 5°S to 5°N, for NoML it was derived without regions where  $Ri \leq 1$ , and for SO it used only the region from 90° to 30°S.

	STD	rdbL	rdbH	gamL	gamH	NoEq	NoML	SO
$D_s$ (TW)	0.31	0.54	0.21	0.49	0.21	0.26	0.25	0.13

As can be inferred from Fig. 7, the downscale energy flux is quite large in the Southern Ocean. In fact, we find that 0.13 TW and thus half of the total potential energy dissipation due to a downscale energy flux occurs in the Southern Ocean (up to 30°S). Therefore, the Southern Ocean together with western boundary currents are likely to be the most important regions for an ageostrophic downscale energy transfer.

## 8. Summary and conclusions

In this study, we show how different dynamical conditions influence the direction of the energy flux in wavenumber space. We use different numerical model configurations of a baroclinically unstable flow system to mimic dynamical conditions ranging from quasigeostrophic to ageostrophic flows. Our model is forced by a restoring of zonally averaged buoyancy, which yields a large-scale source of available potential energy and counteracts the eddy-driven restratification. Energy sinks result from a zonal-mean drag as a large-scale sink of kinetic energy, and viscous friction, which acts predominantly on the smallest scales. Determining the relative strength of the small-scale dissipation with respect to its large-scale counterpart gives information about the efficiency of the flow to feature a downscale energy flux. In addition, we calculate spectral energy densities and fluxes and consider the energy cycle of the model in physical and spectral space to obtain a detailed understanding of the routes to dissipation in a baroclinically unstable flow.

Consistent with other studies (e.g., Lindborg 2005; Waite and Bartello 2006; Capet et al. 2008c; Molemaker et al. 2010), we find an upscale kinetic energy flux for dynamics in quasigeostrophic balance and a downscale energy flux as soon as ageostrophic processes are about to become important. While an upscale energy flux is characteristic for geostrophic turbulence (Charney 1971), the downscale flux might be interpreted as a result of stratified turbulence (Lindborg 2006). In fact, dimensionless parameters like Froude or Richardson numbers derived from our simulations with a downscale kinetic energy flux indicate that these simulations get close to but do not enter the parameter regime that Lindborg (2005) and Waite and Bartello (2006) identify to be characteristic for stratified turbulence. The downscale flux of kinetic energy in the experiments with ageostrophic dynamics comes along with large dissipation rates at the smallest resolved scales by the viscous friction. Therefore, we confirm the results from Capet et al. (2008c) and Molemaker et al. (2010) who find that ageostrophic dynamics are able to yield a direct route to dissipation in contrast to quasigeostrophic dynamics.

Here, we relate the strength of this direct route to the Richardson number  $Ri$  that characterizes the dynamical conditions of our model.

For simulations with large  $Ri$ , the observed dynamics are to a large extent in geostrophic balance. The smaller  $Ri$  becomes, however, the more unbalanced ageostrophic dynamics are evident [see also Stone (1970) and Molemaker et al. (2005)]. These unbalanced dynamics feature a horizontal divergent velocity field. A decomposition of the energy flux into its rotational and divergent components shows a close relation between the energy flux associated with the divergent velocity component and the downscale energy flux. Therefore, we conclude that the strength of the small-scale dissipation directly depends on the strength of the divergent velocity field.

To explain the efficiency of the direct route to dissipation for ageostrophic dynamics, we like to propose the following chain of arguments: If a baroclinically unstable background state of a flow has a low Richardson number induced, for example, by a low stratification or a high vertical shear, the turbulent flow is likely to contain ageostrophic velocity components induced, for example, by frontogenesis (Hoskins and Bretherton 1972), ageostrophic instabilities (Molemaker et al. 2005), or Lighthill generation of gravity waves (Ford et al. 2000). Additionally, the flow tends to be horizontally divergent and following McWilliams (1985); horizontally divergent velocity components grow faster in time as  $Ri$  decreases. As shown, for example, by Capet et al. (2008c) and in this study, the enhanced divergent velocity component at low  $Ri$  is responsible for a downscale kinetic energy flux that counteracts the upscale kinetic energy flux associated with the geostrophic velocity component of the flow. This downscale kinetic energy flux transfers kinetic energy to spatial scales where three-dimensional turbulence sets in and further transfers the energy downscale up to scales where finally the energy is dissipated by molecular friction. Therefore, ageostrophic dynamics are able to induce dissipation by establishing a direct route of kinetic energy toward small scales.

Until now, it is not clear how the energy of the mesoscale eddy field is dissipated. Some possible candidates are bottom friction (Arbic et al. 2009), topographic inviscid dissipation of balanced flow (Dewar and Hogg 2010), lee-wave generation (Bell 1975; Nikurashin and Ferrari 2011), Lighthill generation of gravity waves (Ford et al. 2000), gravity wave drag on the balanced flow (Müller 1976), ageostrophic instability (Molemaker et al. 2005), or the direct route to dissipation by ageostrophic dynamics. While some of the former mechanism might induce internal waves that

transfer energy toward smaller scales by nonlinear wave–wave interactions, the latter needs to be catalyzed by some process that induces ageostrophic dynamics. Thus, the role of the former processes might be twofold, on the one hand by directly dissipating energy or on the other hand by providing ageostrophic conditions for a direct route to dissipation. However, quantification for all these processes is mandatory in order to obtain a more detailed understanding of the energy cycle of the ocean circulation.

The global estimate of the small-scale dissipation induced by a downscale energy flux, made in this study, is a first step to quantify the importance of the direct route to dissipation in comparison to competing processes like, for example, dissipation due to bottom friction (Arbic et al. 2009) or lee-wave generation of internal waves (Nikurashin and Ferrari 2011). Our estimate derived from an eddy-permitting ( $1/10^\circ$  horizontal resolution) realistic global ocean model (von Storch et al. 2012) suggests that presumably  $0.31 \pm 0.23$  TW are dissipated by an ageostrophic downscale energy transfer. This is 31% of the 1-TW wind power input into geostrophic flows in the ocean as estimated by Wunsch (1998) and 17% of the 1.85-TW wind power input into the mean flow as estimated by von Storch et al. (2012) for the underlying model. However, we note that model problems such as the relatively coarse vertical resolution at depth might impact our estimate here, an issue that requires further work.

In comparison, Nikurashin and Ferrari (2011) estimate an energy flux into internal lee waves and thus to dissipation through this process of 0.2 TW. The energy loss due to bottom friction is 0.12 TW in the model simulation used in this study and thus slightly smaller than the estimates for bottom friction of Arbic et al. (2009) ranging between 0.14 and 0.65 TW. Note, however, that the magnitude of the bottom friction strongly depends on the unknown drag coefficient and might be even larger if the effect of tidal currents is included. Zhai et al. (2010) suggest that there is a convergence of eddy energy near the western boundary poleward of  $10^\circ$  in latitude of approximately 0.1 to 0.3 TW. They suggest that this energy might be dissipated due to topographic inviscid dissipation of balanced flow (Dewar and Hogg 2010), but we argue that it might also be dissipated by an ageostrophic downscale energy flux that appears quite efficient in western boundary currents. Using laboratory experiments, Williams et al. (2008) estimate the energy that is extracted from a quasigeostrophic wave and transferred into internal gravity waves by Lighthill radiation. They furthermore extrapolate their results from the annulus experiments to estimate a magnitude of 1.5-TW energy leakage into the gravity wave field by

Lighthill radiation in the real ocean. While the authors admit that their extrapolation is presumably quite crude (e.g., the aspect ratio of their experiments is different than that in the ocean), they conclude that dissipation by Lighthill radiation might play an important role in the ocean energy cycle. All together, these sinks of energy might be sufficient to balance the energy input of 1 TW by the wind. In any case, the results obtained in this study indicate that the direct route to dissipation is likely to play an important role in the ocean energy cycle.

Although our model simulations allow some insights into the different dynamics acting at small and large  $Ri$ , they contain many simplifications in contrast to more realistic flow systems. The zonal-mean drag extracts energy at the basin scale of our model domain. For a model with a larger domain size, we would expect this energy to be transferred further toward larger scales. At these scales, different dissipation mechanisms like, for example, lee-wave generation (Bell 1975; Nikurashin and Ferrari 2011), Lighthill generation of gravity waves (Ford et al. 2000), or ageostrophic instabilities (Molemaker et al. 2005) might play an important role. In our simulations, we prescribe an artificial cutoff of the energy transfer and therefore assume that there is no further backscattering of energy. Furthermore, bi-harmonic diffusion is certainly a more artificial than realistic way to dissipate energy at small scales. However, we assume that the energy flux is more or less independent of the specific realization of the small-scale and large-scale dissipation and that our results would not change for other dissipation schemes.

The restoring of zonal-mean buoyancy is a diabatic process. Since the ocean interior is assumed to be nearly adiabatic, our equilibrated simulations might primarily be seen as a model of the ocean mixed layer where diabatic processes are certainly present. The buoyancy restoring might be replaced by other processes that prevent a restratification of an inclined buoyancy surface to obtain comparable flow conditions in an adiabatic environment. In general, we would expect that our results are also transferable to situations where a geostrophic background state with inclined buoyancy surfaces is retained by a more realistic process than our artificial restoring. We demonstrate in particular that a downscale energy flux can also be found for almost adiabatic flows in section 6, indicating that diabatic forcing plays no great role for this process.

Furthermore, the setup considered in this study intends to simulate horizontally isotropic turbulence since we assume constant values of vertical and horizontal stratification as well as a constant planetary vorticity. Especially for larger scales, however, a change of the planetary vorticity causes a development of zonal jets



and thus a highly anisotropic flow. A characteristic length scale of these zonal jets is the Rhines scale  $L_\beta \propto \sqrt{U/\beta}$ , where  $\beta$  is the change of planetary vorticity and  $U$  is a characteristic velocity scale. The upscale energy cascade of quasigeostrophic turbulence is not necessarily halted at this scale, but the energy spectrum becomes highly anisotropic for larger scales (see, e.g., Vallis 2006) and it is not clear to which extent the results obtained, for example, for the scaling of the large- and small-scale dissipation rates hold for such anisotropic flows. Nevertheless, we do not expect major changes on smaller scales since these are not affected by the  $\beta$  effect as long as their scale is smaller than  $L_\beta$ .

**Acknowledgments.** We kindly acknowledge the very helpful suggestions of two anonymous reviewers. Furthermore, we thank Jin-Song von Storch, Irina Fast, and Helmuth Haak for supporting us with the STORM data. This work was supported by BMBF-SOPRAN FKZ 03F0662E.

## APPENDIX

### Derivation of the Spectral Kinetic Energy Density

To obtain an expression for the spectral kinetic energy density, we first consider the cumulative kinetic energy associated with low-pass filtered velocities (see Frisch 1995):

$$\mathbf{u}_K^< = \sum_{k < K} \widehat{\mathbf{u}}_h^{ikr} e^{ikr}, \quad (\text{A1})$$

where  $k = \sqrt{k_x^2 + k_y^2}$  is the horizontal wavenumber, and  $K$  is a cutoff wavenumber. The globally averaged cumulative kinetic energy  $E_K^<$  then reads

$$E_K^< = \frac{1}{V} \int \frac{1}{2} (\mathbf{u}_K^<)^2 d^3r, \quad \text{and} \quad (\text{A2})$$

$$= \frac{1}{2H} \int \sum_{k, k' < K} \widehat{\mathbf{u}}_h(k) \cdot \widehat{\mathbf{u}}_h(k') \frac{1}{A} \int e^{i(k+k')r} d^2r dz, \quad (\text{A3})$$

and by using  $(1/A) \int e^{i(k+k')r} d^2r = \delta_{k, -k'}$  it can be written as

$$E_K^< = \frac{1}{2H} \int \sum_{k, k' < K} \widehat{\mathbf{u}}_h(k) \cdot \widehat{\mathbf{u}}_h(k') \delta_{k, -k'} dz, \quad \text{and} \quad (\text{A4})$$

$$= \frac{1}{2H} \int \sum_{k < K} \widehat{\mathbf{u}}_h^*(k) \cdot \widehat{\mathbf{u}}_h(k) dz. \quad (\text{A5})$$

From this, we obtain the spectral kinetic energy density by differentiating

$$E_{KE} = \partial_K E_K^<, \quad \text{and} \quad (\text{A6})$$

$$= \frac{1}{2H\Delta K} \int \widehat{\mathbf{u}}_h^* \cdot \widehat{\mathbf{u}}_h dz, \quad (\text{A7})$$

with  $\Delta K = 2\pi/(L_x^2 + L_y^2)^{1/2}$ . Likewise, any spectral tendency  $\widehat{T}_{KE}$  within the balance of  $E_{KE}$  can be derived by the corresponding tendencies  $T_u$  and  $T_v$  of the zonal and meridional momentum equations, respectively:

$$\widehat{T}_{KE} = \frac{1}{H\Delta K} \int (\dot{u}^* \widehat{T}_u + \dot{v}^* \widehat{T}_v) dz. \quad (\text{A8})$$

Equivalently, the spectral tendency might also be expressed in its flux form:

$$\Pi_T(k) = \frac{1}{H} \int \sum_{k < K} (\dot{u}^* \widehat{T}_u + \dot{v}^* \widehat{T}_v) dz. \quad (\text{A9})$$

## REFERENCES

- Arbic, B. K., and Coauthors, 2009: Estimates of bottom flows and bottom boundary layer dissipation of the oceanic general circulation from global high-resolution models. *J. Geophys. Res.*, **114**, C02024, doi:[10.1029/2008JC005072](https://doi.org/10.1029/2008JC005072).
- , K. L. Polzin, R. B. Scott, J. G. Richman, and J. F. Shriver, 2013: On eddy viscosity, energy cascades, and the horizontal resolution of gridded satellite altimeter products. *J. Phys. Oceanogr.*, **43**, 283–300, doi:[10.1175/JPO-D-11-0240.1](https://doi.org/10.1175/JPO-D-11-0240.1).
- Barkan, R., K. B. Winters, and S. G. Llewellyn Smith, 2015: Energy cascades and loss of balance in a reentrant channel forced by wind stress and buoyancy fluxes. *J. Phys. Oceanogr.*, **45**, 272–293, doi:[10.1175/JPO-D-14-0068.1](https://doi.org/10.1175/JPO-D-14-0068.1).
- Bell, T. H., 1975: Topographically generated internal waves in the open ocean. *J. Geophys. Res.*, **80**, 320–327, doi:[10.1029/JC080i003p00320](https://doi.org/10.1029/JC080i003p00320).
- Blumen, W., 1978: Uniform potential vorticity flow: Part I. Theory of wave interactions and two-dimensional turbulence. *J. Atmos. Sci.*, **35**, 774–783, doi:[10.1175/1520-0469\(1978\)035<0774:UPVFI>2.0.CO;2](https://doi.org/10.1175/1520-0469(1978)035<0774:UPVFI>2.0.CO;2).
- Capet, X., J. C. McWilliams, M. J. Molemaker, and A. F. Shchepetkin, 2008a: Mesoscale to submesoscale transition in the California Current System. Part I: Flow structure, eddy flux, and observational tests. *J. Phys. Oceanogr.*, **38**, 29–43, doi:[10.1175/2007JPO3671.1](https://doi.org/10.1175/2007JPO3671.1).
- , —, —, and —, 2008b: Mesoscale to submesoscale transition in the California Current System. Part II: Frontal processes. *J. Phys. Oceanogr.*, **38**, 44–64, doi:[10.1175/2007JPO3672.1](https://doi.org/10.1175/2007JPO3672.1).
- , —, —, and —, 2008c: Mesoscale to submesoscale transition in the California Current System. Part III: Energy balance and flux. *J. Phys. Oceanogr.*, **38**, 2256–2269, doi:[10.1175/2008JPO3810.1](https://doi.org/10.1175/2008JPO3810.1).
- Charney, J. G., 1971: Geostrophic turbulence. *J. Atmos. Sci.*, **28**, 1087–1095, doi:[10.1175/1520-0469\(1971\)028<1087:GT>2.0.CO;2](https://doi.org/10.1175/1520-0469(1971)028<1087:GT>2.0.CO;2).
- D'Asaro, E., C. Lee, L. Rainville, R. Harcourt, and L. Thomas, 2011: Enhanced turbulence and energy dissipation at ocean fronts. *Science*, **332**, 318–322, doi:[10.1126/science.1201515](https://doi.org/10.1126/science.1201515).
- Deusebio, E., A. Vallgren, and E. Lindborg, 2013: The route to dissipation in strongly stratified and rotating flows. *J. Fluid Mech.*, **720**, 66–103, doi:[10.1017/jfm.2012.611](https://doi.org/10.1017/jfm.2012.611).

- Dewan, E., 1997: Saturated-cascade similitude theory of gravity wave spectra. *J. Geophys. Res.*, **102**, 29 799–29 817, doi:[10.1029/97JD02151](https://doi.org/10.1029/97JD02151).
- Dewar, W. K., and A. M. Hogg, 2010: Topographic inviscid dissipation of balanced flow. *Ocean Modell.*, **32**, 1–13, doi:[10.1016/j.ocemod.2009.03.007](https://doi.org/10.1016/j.ocemod.2009.03.007).
- Ferrari, R., and C. Wunsch, 2009: Ocean circulation kinetic energy: Reservoirs, sources, and sinks. *Annu. Rev. Fluid Mech.*, **41**, 253–282, doi:[10.1146/annurev.fluid.40.111406.102139](https://doi.org/10.1146/annurev.fluid.40.111406.102139).
- Fjørtoft, R., 1953: On the changes in the spectral distribution of kinetic energy for twodimensional, nondivergent flow. *Tellus*, **5A**, 225–230, doi:[10.1111/j.2153-3490.1953.tb01051.x](https://doi.org/10.1111/j.2153-3490.1953.tb01051.x).
- Ford, R., M. E. McIntyre, and W. A. Norton, 2000: Balance and the slow quasimanifold: Some explicit results. *J. Atmos. Sci.*, **57**, 1236–1254, doi:[10.1175/1520-0469\(2000\)057<1236:BATSQS>2.0.CO;2](https://doi.org/10.1175/1520-0469(2000)057<1236:BATSQS>2.0.CO;2).
- Fox-Kemper, B., R. Ferrari, and R. Hallberg, 2008: Parameterization of mixed layer eddies. Part I: Theory and diagnosis. *J. Phys. Oceanogr.*, **38**, 1145–1165, doi:[10.1175/2007JPO3792.1](https://doi.org/10.1175/2007JPO3792.1).
- Frisch, U., 1995: *Turbulence: The Legacy of A. N. Kolmogorov*. Cambridge University Press, 296 pp.
- Hoskins, B. J., and F. P. Bretherton, 1972: Atmospheric frontogenesis models: Mathematical formulation and solution. *J. Atmos. Sci.*, **29**, 11–37, doi:[10.1175/1520-0469\(1972\)029<0011:AFMMFA>2.0.CO;2](https://doi.org/10.1175/1520-0469(1972)029<0011:AFMMFA>2.0.CO;2).
- Klein, P., B. L. Hua, G. Lapeyre, X. Capet, S. Le Gentil, and H. Sasaki, 2008: Upper ocean turbulence from high-resolution 3D simulations. *J. Phys. Oceanogr.*, **38**, 1748–1763, doi:[10.1175/2007JPO3773.1](https://doi.org/10.1175/2007JPO3773.1).
- Kolmogorov, A. N., 1991: Dissipation of energy in the locally isotropic turbulence. *Proc. Math. Phys. Sci.*, **434**, 15–17, doi:[10.1098/rspa.1991.0076](https://doi.org/10.1098/rspa.1991.0076).
- LaCasce, J. H., 2012: Surface quasigeostrophic solutions and baroclinic modes with exponential stratification. *J. Phys. Oceanogr.*, **42**, 569–580, doi:[10.1175/JPO-D-11-0111.1](https://doi.org/10.1175/JPO-D-11-0111.1).
- Lindborg, E., 2005: The effect of rotation on the mesoscale energy cascade in the free atmosphere. *Geophys. Res. Lett.*, **32**, L01809, doi:[10.1029/2004GL021319](https://doi.org/10.1029/2004GL021319).
- , 2006: The energy cascade in a strongly stratified fluid. *J. Fluid Mech.*, **550**, 207–242, doi:[10.1017/S0022112005008128](https://doi.org/10.1017/S0022112005008128).
- Lorenz, E. N., 1955: Available potential energy and the maintenance of the general circulation. *Tellus*, **7A**, 157–167, doi:[10.1111/j.2153-3490.1955.tb01148.x](https://doi.org/10.1111/j.2153-3490.1955.tb01148.x).
- Marshall, J., A. Adcroft, C. Hill, L. Perelman, and C. Heisey, 1997: A finite-volume, incompressible Navier Stokes model for studies of the ocean on parallel computers. *J. Geophys. Res.*, **102**, 5753–5766, doi:[10.1029/96JC02775](https://doi.org/10.1029/96JC02775).
- McWilliams, J. C., 1985: Submesoscale, coherent vortices in the ocean. *Rev. Geophys.*, **23**, 165–182, doi:[10.1029/RG023i002p00165](https://doi.org/10.1029/RG023i002p00165).
- Molemaker, M. J., and J. C. McWilliams, 2010: Local balance and cross-scale flux of available potential energy. *J. Fluid Mech.*, **645**, 295–314, doi:[10.1017/S0022112009992643](https://doi.org/10.1017/S0022112009992643).
- , —, and I. Yavneh, 2005: Baroclinic instability and loss of balance. *J. Phys. Oceanogr.*, **35**, 1505–1517, doi:[10.1175/JPO2770.1](https://doi.org/10.1175/JPO2770.1).
- , —, and X. Capet, 2010: Balanced and unbalanced routes to dissipation in an equilibrated Eady flow. *J. Fluid Mech.*, **654**, 35–63, doi:[10.1017/S0022112009993272](https://doi.org/10.1017/S0022112009993272).
- Müller, P., 1976: On the diffusion of momentum and mass by internal gravity waves. *J. Fluid Mech.*, **77**, 789–823, doi:[10.1017/S0022112076002899](https://doi.org/10.1017/S0022112076002899).
- Nagai, T., A. Tandon, H. Yamazaki, and M. J. Doubell, 2009: Evidence of enhanced turbulent dissipation in the frontogenetic Kuroshio Front thermocline. *Geophys. Res. Lett.*, **36**, L12609, doi:[10.1029/2009GL038832](https://doi.org/10.1029/2009GL038832).
- Nastrom, G. D., and K. S. Gage, 1985: A climatology of atmospheric wavenumber spectra of wind and temperature observed by commercial aircraft. *J. Atmos. Sci.*, **42**, 950–960, doi:[10.1175/1520-0469\(1985\)042<0950:ACOAWS>2.0.CO;2](https://doi.org/10.1175/1520-0469(1985)042<0950:ACOAWS>2.0.CO;2).
- Nikurashin, M., and R. Ferrari, 2011: Global energy conversion rate from geostrophic flows into internal lee waves in the deep ocean. *Geophys. Res. Lett.*, **38**, L08610, doi:[10.1029/2011GL046576](https://doi.org/10.1029/2011GL046576).
- Rhines, P., 1977: The dynamics of unsteady currents. *Marine Modeling*, E. D. Goldberg et al., Eds., The Sea, Vol. 6, Wiley, 189–318.
- Scott, R. B., and F. Wang, 2005: Direct evidence of an oceanic inverse kinetic energy cascade from satellite altimetry. *J. Phys. Oceanogr.*, **35**, 1650–1666, doi:[10.1175/JPO2771.1](https://doi.org/10.1175/JPO2771.1).
- Stone, P. H., 1966: On non-geostrophic baroclinic stability. *J. Atmos. Sci.*, **23**, 390–400, doi:[10.1175/1520-0469\(1966\)023<0390:ONGBSP>2.0.CO;2](https://doi.org/10.1175/1520-0469(1966)023<0390:ONGBSP>2.0.CO;2).
- , 1970: On non-geostrophic baroclinic stability: Part II. *J. Atmos. Sci.*, **27**, 721–726, doi:[10.1175/1520-0469\(1970\)027<0721:ONGBSP>2.0.CO;2](https://doi.org/10.1175/1520-0469(1970)027<0721:ONGBSP>2.0.CO;2).
- Tulloch, R., and K. S. Smith, 2009: Quasigeostrophic turbulence with explicit surface dynamics: Application to the atmospheric energy spectrum. *J. Atmos. Sci.*, **66**, 450–467, doi:[10.1175/2008JAS2653.1](https://doi.org/10.1175/2008JAS2653.1).
- Vallis, G. K., 2006: *Atmospheric and Oceanic Fluid Dynamics*. Cambridge University Press, 745 pp.
- von Storch, J.-S., C. Eden, I. Fast, H. Haak, D. Hernández-Deckers, E. Maier-Reimer, J. Marotzke, and D. Stammer, 2012: An estimate of the Lorenz energy cycle for the World Ocean based on the 1/10° STORM/NCEP simulation. *J. Phys. Oceanogr.*, **42**, 2185–2205, doi:[10.1175/JPO-D-12-079.1](https://doi.org/10.1175/JPO-D-12-079.1).
- Waite, M. L., and P. Bartello, 2004: Stratified turbulence dominated by vortical motion. *J. Fluid Mech.*, **517**, 281–308, doi:[10.1017/S0022112004000977](https://doi.org/10.1017/S0022112004000977).
- , and —, 2006: The transition from geostrophic to stratified turbulence. *J. Fluid Mech.*, **568**, 89–108, doi:[10.1017/S0022112006002060](https://doi.org/10.1017/S0022112006002060).
- Williams, P. D., T. W. N. Haine, and P. L. Read, 2008: Inertia-gravity waves emitted from balanced flow: Observations, properties, and consequences. *J. Atmos. Sci.*, **65**, 3543–3556, doi:[10.1175/2008JAS2480.1](https://doi.org/10.1175/2008JAS2480.1).
- Wunsch, C., 1998: The work done by the wind on the oceanic general circulation. *J. Phys. Oceanogr.*, **28**, 2332–2340, doi:[10.1175/1520-0485\(1998\)028<2332:TWDBTW>2.0.CO;2](https://doi.org/10.1175/1520-0485(1998)028<2332:TWDBTW>2.0.CO;2).
- Zhai, X., H. L. Johnson, and D. P. Marshall, 2010: Significant sink of ocean-eddy energy near western boundaries. *Nat. Geosci.*, **3**, 608–612, doi:[10.1038/ngeo943](https://doi.org/10.1038/ngeo943).